Preprint statement: *This is a non-peer reviewed preprint submitted to EarthArXiv. The paper was submitted to Science of the Total Environment 12 July 2024 and is currently under review. New versions of the preprint might contain different content.*

More biomass burning aerosol is being advected westward over the southern tropical Atlantic since 2003

Tyler Tatro[1] and Paquita Zuidema[1]

[1] Rosenstiel School of Marine, Atmospheric, and Earth Science, University of Miami, Miami, FL, USA.

Corresponding author: Tyler Tatro (tyler.tatro@miami.edu)

Highlights:

- Burned area datasets indicate fires are fewer in May but more common in August and September, compressing the southern African biomass burning season.
- Smoke is carried further over the southeast Atlantic due to increased land surface temperatures (thermal wind) and midlatitude jet shifts (tropical expansion).
- Advection of warm, smoky free-tropospheric continental air preserves the southern edge of the stratocumulus deck, despite warming ocean temperatures.

Abstract

Each year, agricultural fires in southern continental Africa emit approximately one third of the world's biomass burning aerosol. This is advected westward by the prevailing circulation winds over a subtropical stratocumulus cloud deck. The radiative effects from the aerosol and aerosol-cloud interactions impact regional circulations and hydrology. Here we examine how changes in the coupled southern African earth system over the past 20 years impact the southeast Atlantic. We combine satellite-derived burned area datasets with ECMWF-reanalysis carbon monoxide, black carbon, and meteorology from the biomass burning season (May-October) in southern Africa. The burning season begins in May in woody savannas in the northwest and shifts to open savanna and grassland fires in the southeast, with small fires (less than 1 km^2) contributing significantly to total burned area. More small fires are occurring in the middle of the biomass burning season and the overall season is shorter, corroborated by reanalysis carbon monoxide fields. Significantly increased free tropospheric winds, shifted southward, transport smoke aerosol further southwest over the southeast Atlantic. The increased aerosol advection is coupled with a southern shift in the south Atlantic subtropical high and an increase in the low cloud fraction on the southern edge of the stratocumulus cloud deck. While smoke emissions sources have not changed significantly, changes in the smoke transport pathway, attributed to increasing surface temperatures in southern Africa and tropical expansion, combined with an altered low cloud distribution, explain how the regional radiation balance has shifted to more top-of-atmosphere cooling in recent decades.

Graphical Abstract

See Attached File

Keywords

Biomass burning; CAMS reanalysis; southern African easterly jet; tropical expansion.

1 Introduction

Southern continental Africa contains approximately 36% of the world's burned area (Giglio et al., 2018) and emits approximately 30% of the world's biomass-burning aerosol (BBA) and black carbon (Van Der Werf et al., 2010). The smoke is advected west from June through October, residing both below and above the subtropical southern Atlantic stratocumulus cloud deck (Adebiyi & Zuidema, 2016; Zhang & Zuidema, 2021). When the smoke is located above the low clouds, the smoke absorbs incoming shortwave radiation and strengthens the cloud-capping inversion, ultimately increasing low cloud cover and 'cooling' the earth's surface (Adebiyi & Zuidema, 2018; Gordon et al., 2018; Herbert et al., 2020). Smoke entrained into the boundary layer can support aerosol-cloud microphysical interactions (Twomey, 1977; Kacarab et al., 2020; Zhang & Feingold, 2023) and cause a cloud 'burn-off' (semi-direct effect) (Hansen et al., 1997; Ackerman et al., 2000; Zhang & Zuidema, 2019) by increasing stability in the boundary layer, decoupling the cloud layer from surface moisture sources (Johnson et al., 2004). Since the radiative budget and low cloud seasonal cycle are sensitive to the presence of the BBA (Lu et al., 2018; Che et al., 2020; Zhang & Zuidema, 2021), multiannual changes in the transport of BBA will also have impacts on the top of atmosphere radiative balance.

In recent years the interactions of the advected smoke with the stratocumulus deck have become extensively studied with satellite and modelling efforts, corroborated with data from the NASA ObseRvations of Aerosols above CLouds and their intEractionS (ORACLES) campaign (Redemann et al., 2021), the U.K. Cloud-Aerosol-Radiation Interaction and Forcing: Year 2017 (CLARIFY) campaign (Haywood et al., 2021), the French-led Aerosol Radiation and Clouds in southern Africa campaign (AEROCLO-Sa) campaign (Formenti et al., 2019), the European Dynamics–Aerosol–Chemistry–Cloud Interactions in West Africa (DACCIWA) project (Denjean et al., 2020) and the Department of Energy Layered Atlantic Smoke Interactions with Clouds (LASIC) field campaign (Zuidema et al., 2018). The in-situ data detailing the aerosol-cloud vertical structure reveal that the smoke is more abundant in the remote marine boundary layer and more absorbing than previously thought (Zuidema et al., 2018; Wu et al., 2020). However, the net radiative effect of the smoke (resulting in a warming or cooling) is not well agreed upon within models (Mallet et al., 2021).

Current climate and earth system models still struggle to accurately represent aerosol absorption and cloud fraction over the southeast Atlantic (Mallet et al., 2021). Underestimation of the aerosol absorption is caused by uncertainty in multiple processes; inadequate aerosol chemical interactions (Brown et al., 2021), strong subsidence of the aerosol layer (Das et al., 2017) and a sensitivity to the BBA vertical structure (Herbert et al., 2020). Emissions inventories calculated by using satellite observations of burned area or fire radiative power (FRP) are often scaled up by climate modelers to match observed MODIS aerosol optical depth (AOD) observations (Che et al., 2020).While new emissions datasets (e.g. FINN2.5-Wiedinmyer et al., 2023) are closer to observed aerosol AOD and total-column carbon monoxide (CO) values over Africa, current datasets still differ by as large as a factor of 4 in organic carbon emissions from southern Africa (Pan et al., 2020).

Even though global fire emissions datasets do not agree on the total burned area, or on the amount of CO produced by SHAF fires (Chen et al., 2023; Griffin et al., 2023), fires are the main source of local CO during the burning season, allowing us to connect CO trends and variability directly to trends and variability in smoke transport, irrespective of absolute CO values. Therefore, reanalysis (aided by satellite-assimilated values of some gaseous species) can be used as a proxy for investigating emissions trends and a qualitative constraint on burned area trends. Current global CO concentrations from biomass burning are the lowest recorded in the past few centuries (Wang et al., 2010), but a recent study by Jouan & Myhre (2024) found a detectable increase in the amount of BBA over the southeast Atlantic in the past two decades. However, the root causes of the increased smoke within the biomass burning season remain an open question.

In this study, we use burned area data along with aerosol & meteorological reanalysis to compare the recent trends in fire distribution, meteorology, and cloud response over southern continental Africa (SHAF, defined as 0-30°S) and the southeast Atlantic, during the period 2003-2020. We focus on this period since observations from the *Aqua* and *Terra* satellites are assimilated into reanalysis data after 2002. However, since meteorological reanalysis extends further back, we contextualize recent fire trends with 40-year trends (1980-2020) in reanalysis winds, humidity, and temperature.

2 Data, Methods, and Seasonal Overview

2.1 Burned Area Data

Both burned area and FRP yield insights into burning conditions, but burned area provides a straightforward constraint on fire activity that is less subject to satellite overpass time and cloud obscuration errors (Boschetti et al., 2019). The availability of satellite-derived burned area data products has grown in the last few decades, but the inability of these retrievals to accurately capture small fires (<1 km^2) significantly influences estimates of burned area, particularly in continental Africa (Roteta et al., 2019), where many fires are small, daytime-only, agricultural fires. These contrast to the ‘mega-fires’ of the northern hemisphere from the recent decade. In a study comparing high-resolution burned area (20 m) derived from the Sentinel-2 Multispectral Instrument against other 500-m resolution data products derived from MODIS, Ramo et al. (2021) found an 80% increase in burned area over Africa for 2016 when compared to burned area derived from Terra and Aqua MODIS sensors alone. These differences impact trend estimates–previous literature based on 500m data suggests a decreasing trend in burned area during 2003-2017 in central southern Africa between 0-15°S (Jiang et al., 2020) and during 1997-2016 over 0-30°S (Andela et al., 2017), driven by less fires in savannas and grasslands. GFED5 corroborates declining fires in savannas and grasslands in the past 20 years, but the significance and magnitude of the burned area trend depends on the analyzed time period (Table 5 in Chen et al., 2023).

Given the significance of these small fires, we compare two fire datasets as baselines for constraining the source emissions of biomass burning aerosol. The FireCCI51 data product (Lizundia-Loiola et al., 2020), developed by the European Space Agency’s Climate Change Initiative Program, uses an additional near-infrared channel within MODIS and an alternative cluster-based thresholding algorithm to capture more of the small fires than do other MODIS-derived products (for July and September 2016), but ultimately FireCCI51 uses MODIS 250-meter data to calculate burned area. The Global Fire Emissions Database version 5 (GFED5, Chen et al., 2023) combines MODIS with higher-resolution Landsat and Sentinel 2 burned area datasets to apply historical corrections to account for previously missed small fires. Both datasets are the most recent burned area products available for 2003 to 2020 that detect more fires over southern Africa than the standard MODIS product (MCD64A1). The comparison of the two products is one way to constrain the uncertainty of accounting for small fires.

Both datasets are available on a 0.25x0.25° grid but use different underlying land classification systems. We use both products to contextualize recent trends, but only the GFED5 product to examine monthly changes in burned area by land cover class, as the scaling for small fires should provide a more conservative estimate of recent trends. The GFED5 land classes are based on a modified International Geosphere-Biosphere Program classification following Van Wees et al., (2022).

2.2 Aerosol and Gas Data

We use monthly-averaged carbon monoxide (CO) and black carbon (BC) fields from the ECMWF's Atmospheric Composition Reanalysis 4 (CAMS, Inness et al., 2019) to investigate smoke trends. CO is used as the tracer for biomass burning emissions due to its relative atmospheric lifetime of weeks to months (Holloway et al., 2000). CO emission trends from BBA are masked by global and local anthropogenic trends from industrial centers, but are better constrained by observations than BC, which has a shorter lifetime due to deposition. Western Africa has experienced a large population growth centered near the Gulf of Guinea (Moriconi-Ebrard et al., 2016), but biomass burning remains the largest source of total CO emissions from June to October in southern hemisphere Africa (Liousse et al., 2014).

A comparison of ORACLES flight data to the Modern-Era Retrospective Analysis for Research and Applications version 2 (MERRA-2) reanalysis (Gelaro et al., 2017) and the CAMS reanalysis by Pistone et al. (2024) showed that CAMS specific humidity and CO correlate substantially better with observations than do the MERRA-2 fields. CAMS CO fields are provided at a 0.75x0.75° spatial resolution, with 25 vertical levels (7 levels between 1000 and 500 hPa). BBA emissions in CAMS are driven by the Global Fire Assimilation System (GFAS) version 1.2 (Kaiser et al., 2012), which typically produces lower CO emissions than other datasets (Wiedinmyer et al., 2023). Version 6 total column CO retrievals derived from the thermal infrared band of the Measurement of the Pollution in the Troposphere (MOPITT v.6) instrument are also assimilated into the CAMS reanalysis. CAMS CO concentrations have compared well to satellite and aircraft values over long trajectories (Johansson et al., 2022; Ceamanos et al., 2023) and over seasonal and diurnal variations in black carbon and CO at select locations (Ding & Liu, 2022).

The MOPITT weighting function is more sensitive to upper-altitude CO (300-700 hPa) than lower levels over both oceans (Deeter et al., 2003) and over tropical African rainforests (Deeter et al., 2007), therefore, we reduce the uncertainty in CAMS CO introduced from data assimilation by separately integrating mid-tropospheric CO (500-700 hPa) and lower tropospheric CO (700 to 1000 hPa) to analyze smoke carried by free tropospheric winds and smoke advected near or within the boundary layer. We define these quantities as

$$CO_{MT} = -\int_{700\,hPa}^{500\,hPa} CO_i dp\,; CO_{LT} = -\int_{1000\,hPa}^{700\,hPa} CO_i dp$$

where CO_i represents the mass fraction of CO. The 500-700 hPa altitude captures the bulk of the lidar-derived aerosol vertical distribution from ORACLES measurements over the ocean (Redemann et al., 2021) in August through October, but the altitude of maximum CO concentration is lower (800 hPa) in May through July. CO_{LT} and CO_{MT} together contain ~76% of the total column CO over the continent (10°-40°W, 5°-20°S) and ~68% over the ocean (10°E-10°W, 5°-20°S) from June through October. CO_{LT} contains the majority of CO over the ocean in each month (~42%), although the true percentage is likely higher due to CAMS underestimating CO in the lower troposphere (Inness et al., 2022). However, CAMS CO values in the remote boundary layer match the variability of LASIC observations at Ascension Island ($r^2 = 0.64$ and r^2=0.60, for 2016 and 2017, Figure S1). We similarly analyze black carbon (BC) from CAMS, taken as the sum of the hydrophilic and hydrophobic black carbon mass tracers.

CO levels have decreased globally from 2000 to 2020 caused by improvements in combustion technology (Novelli et al., 2003; Zheng et al., 2019; Buchholz et al., 2021). Therefore, we first isolate smoke transport changes over Africa from the background global reduction in CO. We estimate the global average CO column linear trend from the monthly anomalies averaged between 60°S to 60°N and over all longitudes, then subtract it from the monthly CO fields. We maintain the vertical partitioning of the reanalysis by adjusting the total column reduction so that it is proportional to the mass fraction of CO at each location, time, and altitude.

2.3 Meteorological and Cloud Data

Low cloud cover fraction over the southeast Atlantic is primarily dictated by sea surface temperature (SST), estimated inversion strength (EIS;Wood & Bretherton, 2006) and surface-level, cold air advection (Seethala et al., 2015; Adebiyi et al., 2015; Scott et al., 2020). However, since smoke aerosol can serve as cloud condensation nuclei

(Zuidema et al., 2018; Kacarab et al., 2020), increased cloud droplet number concentrations resulting from smoke intrusions into the cloudy boundary layer can increase cloud brightness (for the same liquid water path) and lengthen cloud lifetimes by suppressing precipitation (Christensen et al., 2020), or possibly promote cloud breakup through enhanced entrainment if droplets become small enough (Bretherton et al., 2007; Diamond et al., 2022). Monthly-mean low cloud fraction and low cloud liquid water path, at a one-degree spatial resolution, come from the Clouds and the Earth's Radiant Energy System (CERES) CldTypHist_Ed4A product (1x1°) (Wielicki et al., 1996). The data product combines Terra-MODIS and Aqua-MODIS retrievals based on the CERES SYN1deg Ed4A retrievals (Winker et al., 2009). Low clouds possess cloud top pressures greater than 680 hPa and any optical depth greater than 0.

Daily cloud droplet number concentration (N_d), from Gryspeerdt et al., (2022) relies on the MODIS collection 6.1 cloud optical properties retrieval dataset (MOD06_L2) for both the Aqua and Terra satellites (Platnick et al., 2017). We compute the monthly average N_d following Grosvenor et al. (2018), which uses the MODIS standard 2.1 μm retrieval and requires a cloud droplet effective radius greater than 4 μm, a cloud optical depth greater than 4, a 5 km cloud fraction greater than 0.9, a solar zenith angle less than 65°, a satellite viewing zenith angle less than 55°, and a cloud mask sub-pixel homogeneity index less than 30. These conditions help capture N_d values closest to aerosol-activated values while removing biases from cloud 3D effects, multiple scattering, partly cloudy pixels, and mixing with environmental air, but N_d selection is not restricted further to the top 10% of the optically-thickest clouds, or by a specific ordering of the effective radius retrievals by wavelength. These criteria capture approximately 65% of the daily N_d values on a 1x1°grid over the southeast Atlantic during each month. For more detail on N_d temporal coverage, see supplementary figures S2 and S3.

Monthly-averaged meteorology (winds, temperature, humidity) is established by ECMWF's Reanalysis 5 (ERA5, 0.25x0.25°) over 1980 to 2020 (Hersbach et al., 2020). We calculate monthly anomalies before computing the least-squares regression slope for each parameter and compare them separately to burned area trends.

2.4 Seasonal Overview

The fires over Southern Africa are primarily small and human-initiated, intended to prepare land for grazing through burning grasses, leaving fire-adapted trees intact, and to a lesser extent burn previously slashed trees (van Wilgen et al., 1990). A clear diurnal cycle, with more burning occurring during the day (Giglio et al., 2006; Roberts et al.,

2009) facilitates the detection of burned areas using satellite visible imagery (Giglio et al., 2003). Over 90% of the annual burned area in southern Africa occurs between June 1 to October 30, with 48% of the annual total burned from August 1 through October 31 in both GFED5 and FireCCI51 datasets. Fires begin in May in northern Angola and in the Democratic Republic of Congo (DRC) and move southeast through the end of October (Fig. 1a), which generally follows the drying pattern of the vegetation (Korontzi, 2005). Since this period coincides with the dry season (Fig. 1c), the semiarid regions further south (10-20°S) are affected by interannual variations in rainfall; wetter years tend to increase fuel availability and burned area during the following burning season (Anyamba et al., 2003).

The seasonal cycle in burning conditions changes the ratio of CO within BBA emissions. Fires at the beginning of the season burn less efficiently than peak season fires, since they consume forested areas with more saturated vegetation and woodier materials (Korontzi, 2005, Dobracki et al., 2024). As the season continues into July and August, fires burn a higher percentage of dry grasses. These undergo more complete combustion and result in a peak in burning efficiency as measured by fire radiative power (Zheng et al., 2018) and the modified combustion efficiency, defined as the ratio of CO_2 to CO_2 and CO (Ward et al., 1996). The annual cycle in total burned area leads that in column CO by one month, so that the peak in burned area occurs in August, while the peak in average total column CO occurs in September (Fig. 1b), averaged over southern Africa. One explanation may be a shift from flaming to more smoldering fires in September-October, when more of the dry grassy fuel is already consumed, leaving woodier materials to burning (Van Der Werf et al., 2006), combined with the return of rainfall (Fig. 1c). Another explanation is that the long chemical lifetime of CO and increased transport from other biomass burning regions delay and shift the peak in CO concentrations to September (van der Velde et al., 2024).

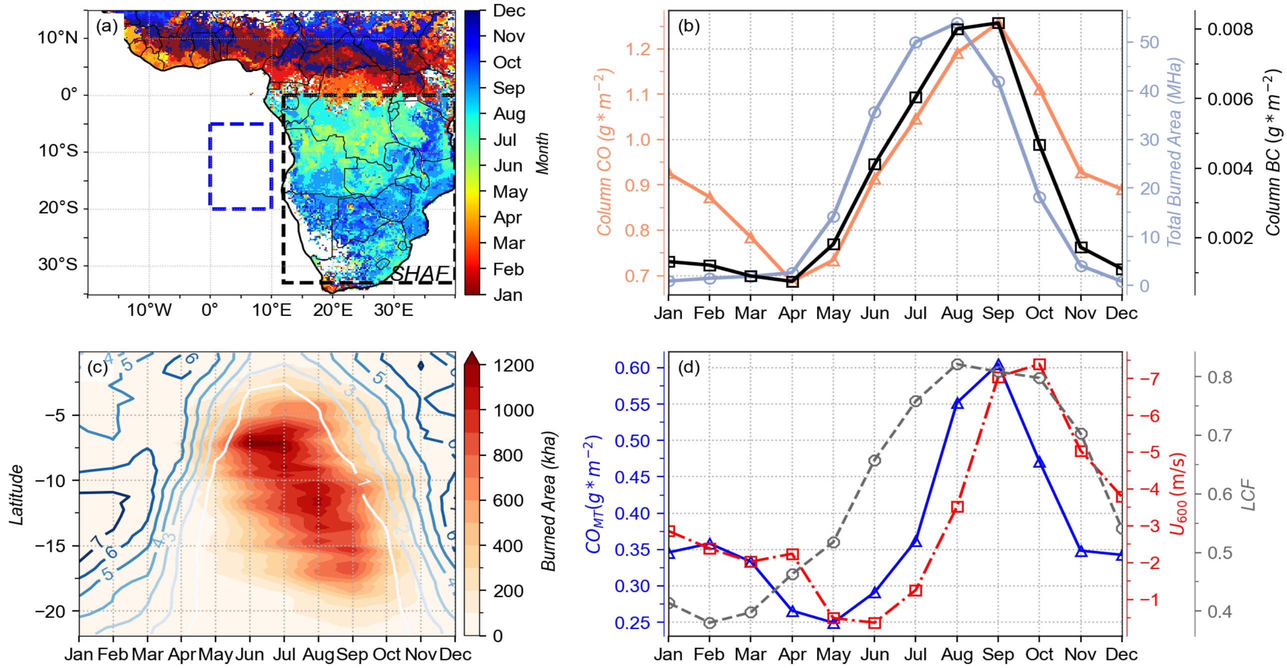

Figure 1. Seasonal cycle of **(a)** monthly maximum in GFED5 burned area, **(b)** CAMS total column CO(orange line) averaged over SHAF and GFED5 total burned area (blue line) summed over SHAF (black box in panel a), **(c)** GFED5 burned area (colored contour) and global precipitation climatology project precipitation (blue lines, 1mm*day^{-1} contours) averaged over 12-40°E and **(d)** CAMS column CO between 800 and 500 hPa (blue triangles), ERA5 zonal wind at 600 hPa (red squares), and CERES low cloud fraction (black circles) averaged offshore (5-15°S, 0-10°E, blue box in panel a).

The large-scale meteorology combines with the fire emissions to transport smoke westward, with synoptic modification from, e.g., mid-latitude disturbances either encouraging further direct zonal transport reaching as far as south America (Holanda et al., 2020), or, a counterclockwise recirculation in the flow field of the Botswana high (Adebiyi & Zuidema, 2016; Kuete et al., 2020). As the continent warms in the spring, a meridional surface temperature gradient between the moist Congo and the hot, dry Kalahari causes a thermal wind balance response (Nicholson & Grist, 2003; Adebiyi & Zuidema, 2016). This response creates an annual maximum in mid-tropospheric easterlies (Fig. 1d), known as the Southern African Easterly Jet (AEJ-S), defined as a monthly easterly windspeed exceeding 6 m/s between 5 and 15°S, which is actively maintained by the mid-tropospheric high over the Kalahari. The jet core moves south and increases in altitude from 700 hPa in August to 600 hPa in September and October as land heating increases over the Kalahari (Ryoo et al., 2021).

The altitude of BBA transport also increases seasonally as the jet carries smoke higher and further west in September and October, when the stratocumulus cloud deck is broader and thicker (Fig. 1d, Ryoo et al., 2021). In July and August, higher smoke concentrations within the boundary layer alter the near-surface radiative heating profile and decrease low cloud fraction near Ascension Island (8°S, 14.5°W) (Zhang & Zuidema, 2019; 2021). In September and October, the higher altitude of BBA promotes low cloud fraction by stabilizing the lower troposphere and reducing incoming shortwave radiation (Wilcox 2010; Adebiyi et al., 2015; Adebiyi & Zuidema, 2018).

3 Results

3.1 Steady Continental Emissions but a Changing Fire Seasonality

Burned area within the first half of the biomass burning season (Figure 2) is comprised of fires in open savannas near the southern edge of the rainforest in the DRC and in the north of Angola. May shows a significant total decrease in burned area (-0.36 Mha or -2.5% of monthly total per year) as fires in tropical forests, woody savannas, and open savannas all contribute to the decreasing trend (Fig. 2a). The gradual decrease in May is centered near the northern Angola-DRC border (Fig. 2b) in the Lunda Norte and Malanje provinces (Catarino et al., 2020), and in the Kasai province of the DRC. Both June and July show significantly less fires in woody savannas, and slightly increased burned area in open savannas, which combine for a negative but insignificant net burned area trend for both months (-0.027 and -0.083 Mha per year, respectively).

June shows increased burned area in the central DRC, slightly east of the areas decreasing in May, consistent with increased forest clearing rates for small-scale rotational agriculture (Tyukavina et al., 2018), and the negative correlation of burned area with population density in this location (Andela et al., 2017). The June increases also mirror the trends found by Wimberly et al., (2024), indicating strong correlations of burned area with maximum temperature and vapor pressure deficit at this location. A combination of meteorological and population changes in the wake of internal displacement from conflict (UNHCR, 2023) are likely fragmenting the landscape, since less of the forest loss is associated with fire over time (van Wees et al., 2021). This reduces fire size and shifts the locations of burning, causing a significant reduction in May and increase in June. Significant decreases in July are concentrated in northeastern Tanzania near game reserves, which we speculate reflects forestry management practices (Ract et al., 2024).

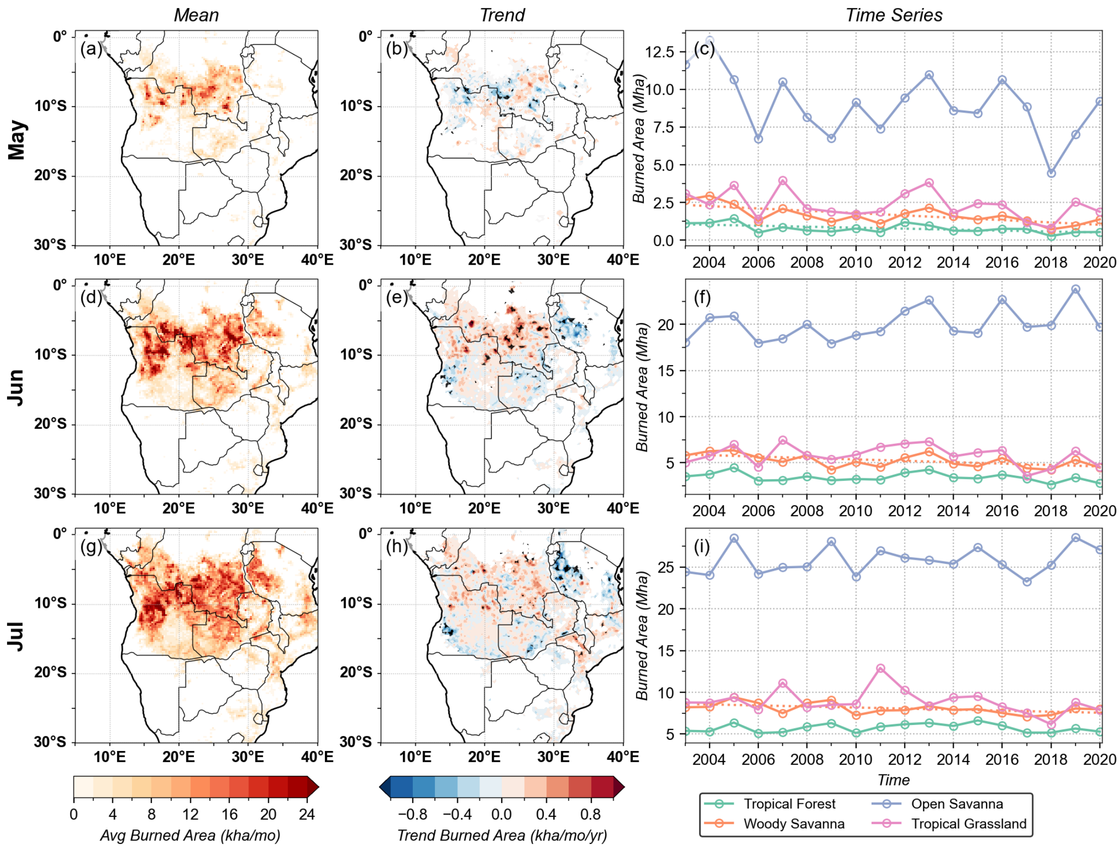

Figure 2. Spatial plots of mean burned area **(a,d,g)**, trends (**b,e,h**), and linear time series of burned area **(c,f,i)** by vegetation class for May-July from 2004 to 2020. The y-axis range in panels c, f, and i differ. Black stippling on panels (b,e,h,) and time series with dashed linear fits indicate significant trends at the 95% confidence level.

In the second half of the season (Figure 3), the proportion of fires in tropical grasslands increases from August (20%) to October (26%) as the fires move southeast. In August, growth in savanna fires (0.19 Mha/year) slightly outpaces significant decreases in grassland fires (-0.13 Mha/year) and other classes, resulting in a near-zero net trend (.032 Mha /year). Fire_CCI shows the largest deviation from GFED5 burned area trends (Figure S4) in August (-0.46 Mha/year). If GFED's scaling for small fires is accurate, then this discrepancy can be understood as an increase in small fires in the month of August. Even though the detection of small fires should extend the traditional fire season (Ramo et al., 2021), August and September (0.12 Mha/year) are the only burning season months with net increasing (but insignificant) burned area trends in GFED5.

Both datasets show decreases in October, when the fires are concentrated in northeast Zambia and along the coast of Mozambique (Fig. 3e, h). Spatial maps of the monthly trends reveal that burned areas increase at these locations in September as well– suggesting that these locations are burning earlier. This may reflect a combination of both fire management practices encouraging earlier burns in the season, and human encroachment favoring deforestation for croplands (Phiri et al., 2023), but this explanation remains speculative. Overall, increased burning in September combined with decreased burning in October act to amplify the seasonal cycle.

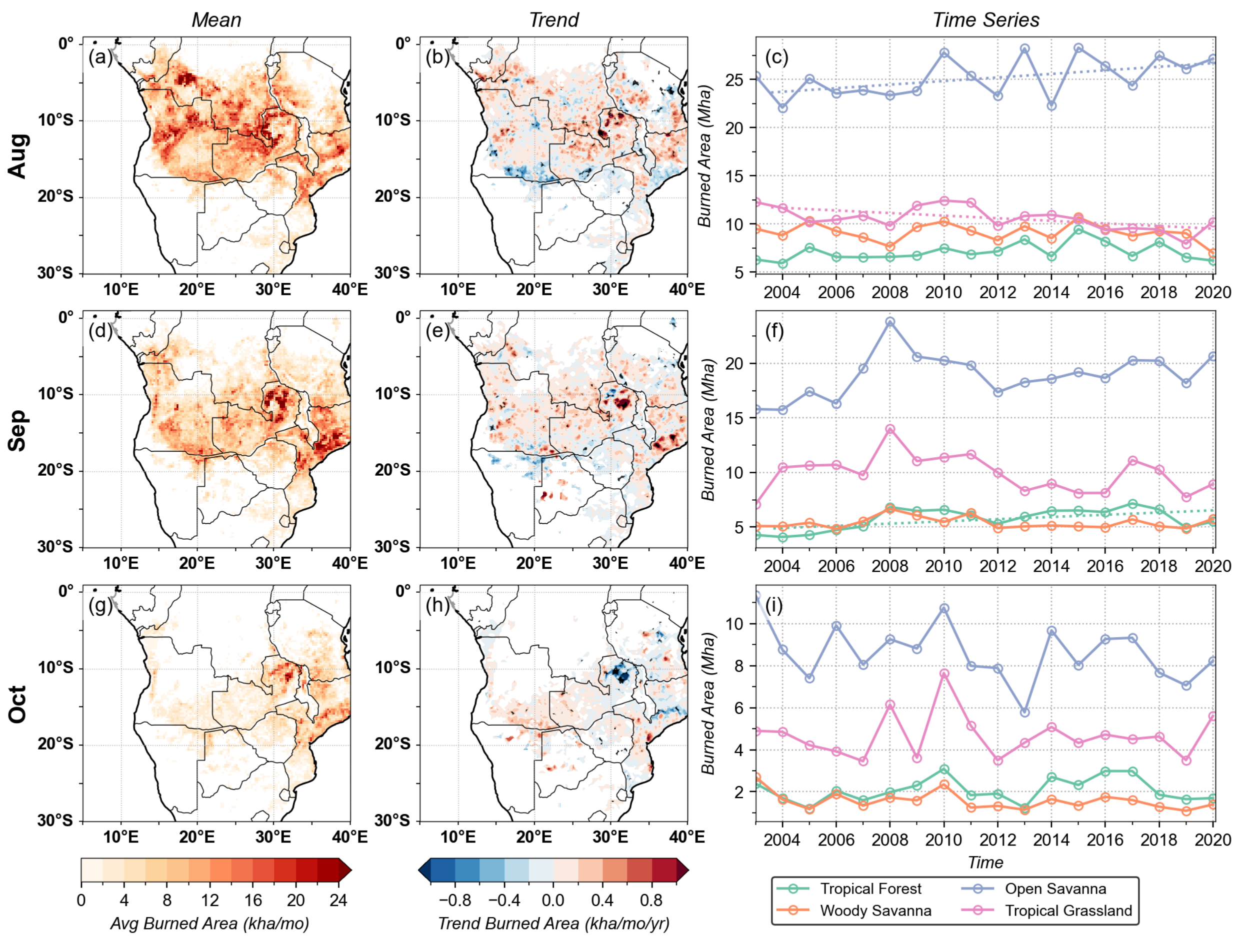

Figure 3. Same as Figure 2 but for August-October.

The decreases in burned area in May and October and increases in open savanna fires in August and September, compress the biomass burning season in time, but with a more amplified ‘peak’, shifted to slightly later in the year (Figure 4a). CO and black carbon in the lower troposphere (the integral from the surface to 700 hPa; Figs 4b and c) corroborate the decline in burned area in May and the increase outside of the biomass burning season from increased anthropogenic emissions (Liousse et al., 2014). In August near 11°S, there is a modest but insignificant uptick in black carbon (Fig. 4c), indicating GFAS may be detecting part of the increase in burned area. The lack of a CO signal in August and September could also stem from proportionally more dry grass fires that burn hotter, and proportionally emit less CO.

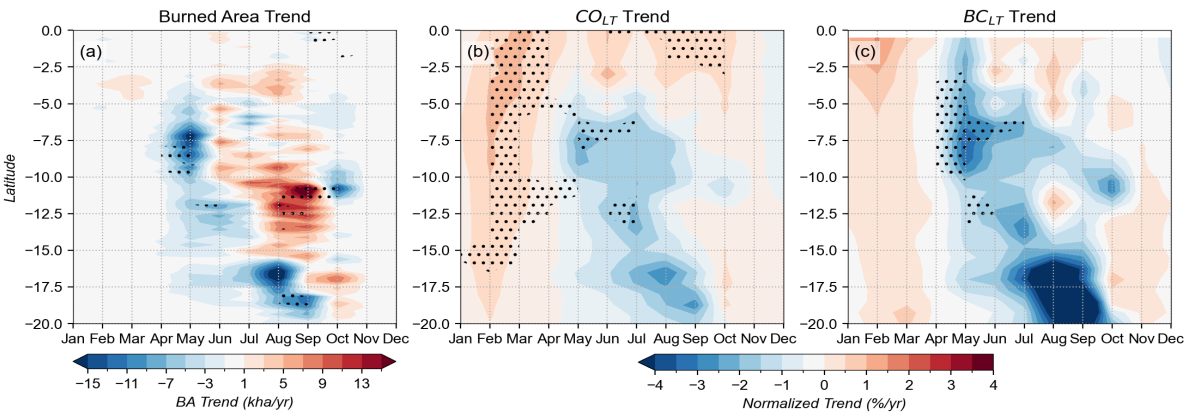

Figure 4. Trends in **(a)** GFEED5 burned area**, (b)** residual CO in the lower troposphere, and **(c)** black carbon in the lower troposphere. Black stippling significant trends at the 90% confidence level.

Despite seasonal changes, the annual average GFED burned area and total column CO (Figure 5) are approximately constant from year to year (coefficients of variation of 3.7% and 3.4%, respectively). The Fire_CCI burned area estimate begins to decrease after 2011 for southern Africa (Fig. 5a), with a total slope of -1.2 Mha (-0.8%) per year, which is slightly less than the decreases found by Jiang et al. (2020). GFED5-estimated burned area is 40% higher than Fire_CCI estimates, and, importantly for this study, GFED does not show a strong decrease in burned area after 2011 (total trend of -.07 Mha or -.035% per year). This illustrates the uncertainty of accounting for small fires. Jiang et al (2020) find no trend for fires smaller than 100 ha, but if GFED's scaling for small fires are accurate, then the difference between the two datasets is primarily because the number of small fires has been increasing since 2010.

The CAMS season-average total column CO and BC over southern continental Africa correlate well with GFED5 (r=0.68 and r=.78, respectively), and Fire_CCI (r=0.59 and r=.76, respectively) burned area, but lack the significant global decrease shown by the global area average of column CO (Fig. 5b). Background CO concentrations during the burning season over continental Africa are too high to be strongly affected by the global reduction, but we see interannual values altered by global signals. An example is the peak in the extreme El Niño summer of 2015 associated with equatorial zonal transport from peat fires in Indonesia (Field et al., 2016) in both the local and global signals. The global CO average reduces in 2008 as a consequence of the economic recession (Yurganov et al., 2010) and never recovers, attributed to improvements in combustion technology and higher air quality standards. Black carbon significantly decreases from 2012 to 2020 (-3.7% per year, $p<.001$), indicative of changes in fire activity, likely driven by the recent wintertime droughts in southern Africa (Wolski et al., 2021).

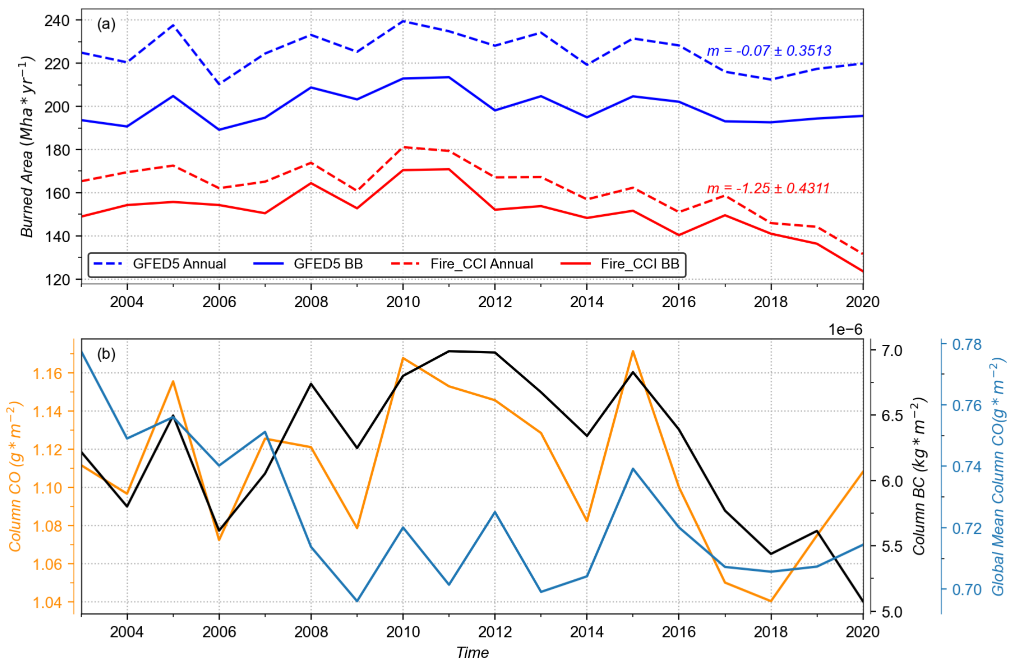

Figure 5. Time series of **(a)** Total burned area in the GFED5 dataset (blue line) and Fire_CCI dataset (red line) annually (solid lines) and between June-October (dashed lines), and **(b)** Vertical integrals of CO and black carbon averaged between 0-30°S, 12-40°W

3.2 Zonal Wind Increases in the Lower Free Troposphere

Easterly winds in the second half of the biomass burning season have increased in strength and width over the past 40 years (1980-2020; Figure 6 a,b,c). AEJ-S winds in August do not increase significantly (-0.002 m/s per year) but demonstrate a southern shift (-0.026 ± .0075° per year, $p < .005$) in the latitude of maximum easterly wind speed (Figures S5 and S6). Average jet speeds increase in September (-0.01 m/s per year) and October (-0.02 m/s per year) as the environmental easterly wind increase (brown shading; Figure 6 d,e,f) is concentrated near the mean jet location (pink contours). This also allows the jet latitudinal width to expand (.06°/year , $p < .05$ and .10°/year, $p < .01$ in September and October, respectively). Increases in easterly wind speed are also more prominent above the mean jet altitude in August and September, although the altitude of maximum AEJ-S speed does not exhibit a detectable increase.

The increase in easterly wind is concentrated on the northern side of the shifting subtropical jet noted in Manney & Hegglin (2018) and Woollings et al., (2023). The westerlies associated with the storm tracks at 30°S have also increased in speed (green shading), thereby increasing the latitudinal gradient in zonal wind, more notably in September and October. The increased heating near the mean location of the surface heat low (red contours) between 1000 and 600 hPa and 15°S-25°S is prominent in all three months and increases in relative strength from August (0.35%) to October (0.64%).

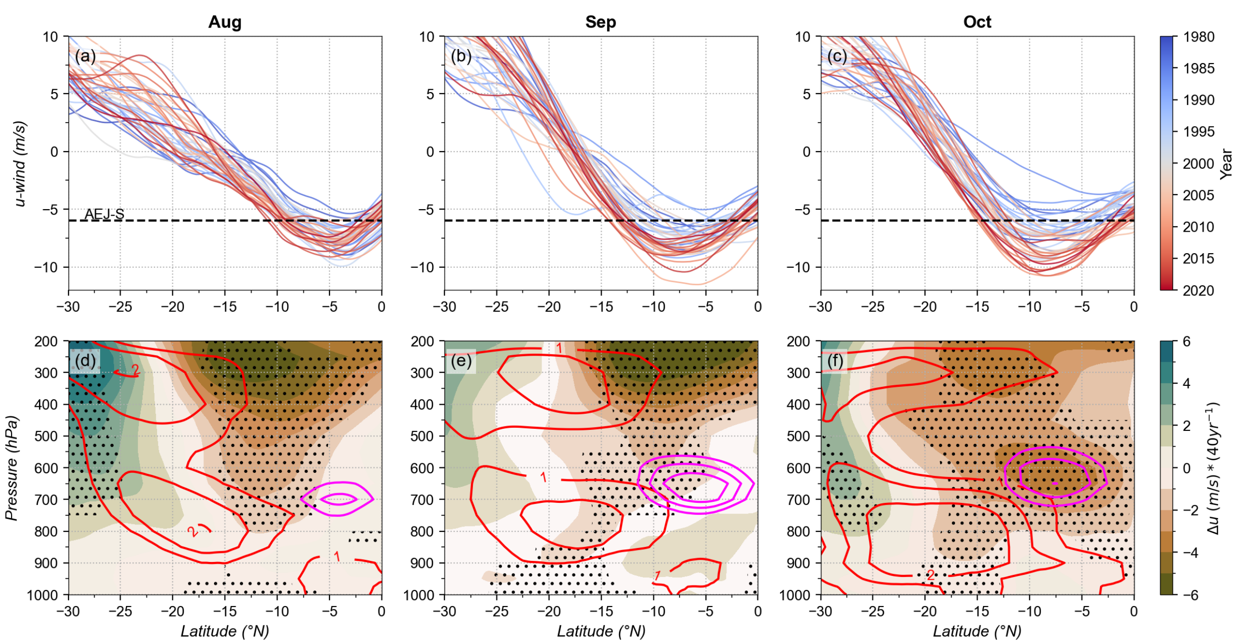

Figure 6. Top row: Monthly-mean u-wind profile at 700 hPa, 600 hPa, and 600 hPa color-coded by year for **(a)** August, **(b)** September, and **(c)** October. Bottom row: Height versus latitude 40-year trends in zonal velocity (u; shading) and trends in heating (red contours, 1,1.5,2 K) and the mean AEJ-S contours (pink, -6 to -8m/s) for 2003-

2022 (bottom row), averaged over 0-25°E. Stippling indicates significance of u-wind trend at the 95% confidence level.

The strengthening and southward shifting of the AEJ-S can be understood as the consequences of two separate long-term changes: a strengthening of the thermal wind through the warming of the southern African continent, and a poleward expansion of the Hadley circulation that is preferentially supporting more warming towards the south. We consider the monthly mean thermal wind change by approximating the vertical wind shear as:

$$U \simeq \frac{-R_D}{f} * \frac{\partial \langle T \rangle}{\partial y} \ln\left(\frac{p}{p_s}\right)$$

where U is the zonal wind at 600 hPa (700 hPa for August), R_D is the dry gas constant, f is the Coriolis parameter, $\langle T \rangle$ is the vertically averaged temperature, y is the latitude, p is the pressure at the jet level, and p_s is the pressure at the surface (1000 hPa). We assume the contribution from the surface wind is negligible for this exercise, so that the thermal wind magnitude is also equal to the wind approximated from geostrophic balance. The independently calculated trend in thermal wind captures the relative magnitude of the zonal wind change, despite overpredicting the ERA5 zonal wind trend over land and underpredicting it over the ocean (Figure 7) in all three months. Even though the correlation between jet intensity and the meridional surface temperature gradient increases from September to November (Kuete et al., 2023), September shows a stronger agreement over land than October. The spatial trends in temperature (Figure S7) reveal warming near the southern edge of the Congo Basin Rainforest during May-October and a larger heating signal concentrated along 20°S around the Kalahari Desert in August to October. These warmer temperatures are being advected over the ocean, which maintains the meridional temperature gradient and supports the AEJ-S increase over the ocean.

The thermal wind budget does not consider momentum contribution from other sources, such as the winds associated with the south Atlantic subtropical high. We attribute the difference between the idealized wind and observed trend to the neglect of other momentum fluxes that can affect the easterly wind – such as the poleward shift of the storm tracks (J. Lu et al., 2007) reducing intrusions from midlatitude disturbances (Kuete et al., 2020), or increased easterlies over the ocean connected to the movement of the south Atlantic subtropical high (Vizy & Cook, 2016). Since changes in the jet speed are larger over the ocean in each month and more significant in September ($p=0.04$) and October ($p=0.005$) than August ($p=0.26$) in both ERA5 and the thermal wind equation, we suspect the southward movement of the South Atlantic High and warmer land surface temperatures encourage stronger easterlies over the ocean at 700 hPa during these months.

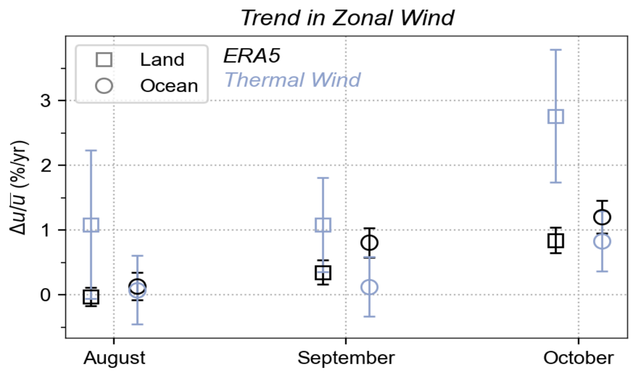

Figure 7. Monthly trends in jet speed between ERA5 (black) and thermal wind (gray) over land (squares, 10-30°W) and ocean (circles, -5-10°W) normalized by the monthly mean zonal wind in each region. The jet region is defined as the 1980-2020 average domain in each month exceeding -6 m/s.

3.3 Increasingly Smoky SEA Free Troposphere

Increased advection is transporting more smoke across the basin in all 3 months (Fig. 8). Increases in BBA during August and September are most prominent over the stratocumulus cloud deck and are more closely linked to the southern African fire sources. Buchholz et al. (2021) and Jouan & Myhre (2024) find similar increases in AOD and in residual total-column CO in the same location. In August, the center of the AEJ-S appears less smoky, which we attribute to a southern shift in the mean location of the jet itself (section 3.2). All three months show positive CO trends north of the equator from urbanization in western Africa. Positive residual trends in CO_{MT} in May through July (Figure S8) in Western Africa and south of 20°S are linked to detrending the global CO reduction, although July shows increases (statistically insignificant) over the mean location of the stratocumulus cloud deck.

Positive trends in CO_{LT} (Figure S9) mirror trends in CO_{MT} for July to October but lack statistical significance in areas associated with biomass burning. Recent work has shown that a fraction of CO (between 0.2 to 0.6) over continental Africa in August-October results from transport from other regions and long CO residence times (van der Velde et al., 2024), but increasing trends in BC_{LT} in July through October (Figure S10) in the same location as CO increases (over the ocean) confirm that local BBA is contributing to the CO trends. The exact contribution of increased CO from African biomass burning versus outside sources remains outside the scope of this work, however.

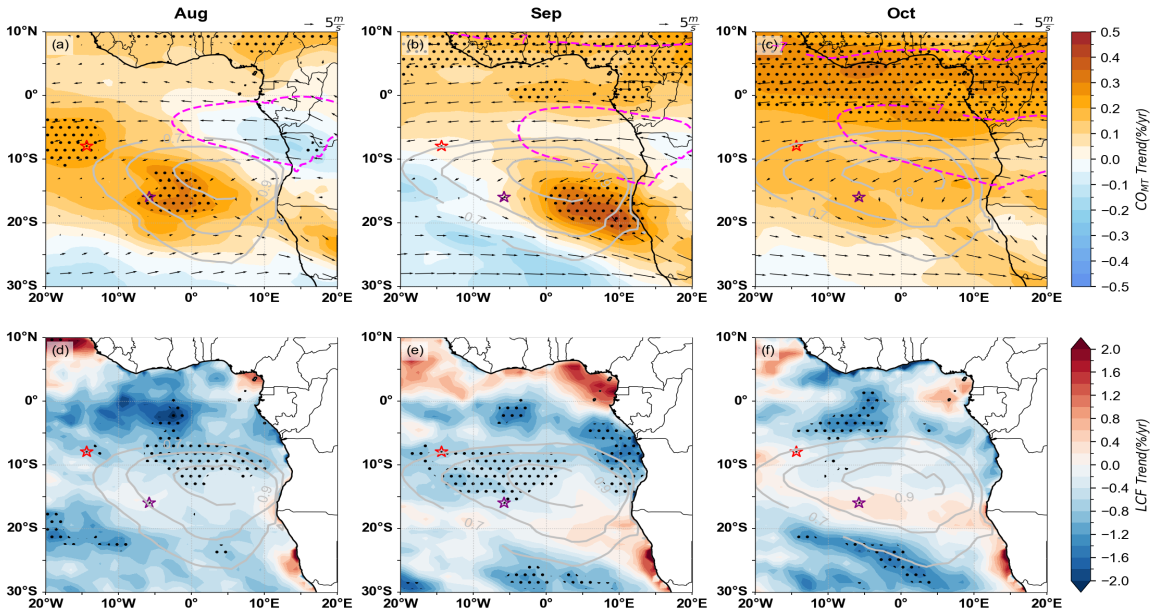

Figure 8. Residual trend in CO_{MT} for a) August, b) September, and c) October (shaded) expressed as a percentage of the CO column mean, shown with the mean jet locations ($|u|>6,7,7$ m*s^{1}, dashed pink contour), mean circulation at the AEJ-S(700, 600, 600 hPa) (vectors) and mean low cloud fraction (gray contours, 0.7-0.9) for 2003-2022 (a-c). Panels d-f indicate the corresponding trend in CERES low cloud fraction. Stippling indicates significance of the regression line at the 95% confidence level. Ascension and St. Helena islands indicated (light and dark red stars).

3.4 Impact on the Southeast Atlantic Stratocumulus Deck

Figure 8 shows a clear delineation between the region with increased mid-tropospheric CO and the thinning northern edge of the stratocumulus cloud deck. Spatial maps of the dominant meteorological parameters that control low cloud fraction (SST, EIS, 900 hPa temperature advection) along with LWP and N_d trends (Figure 9) indicate the sea surface temperature is warming where the low cloud is decreasing in all three months, most notably at the northern edge of the stratocumulus deck, and in October. A strengthening in the low-level, cold temperature advection becoming approximately matches with those regions where the cloud fraction is increasing further south. in September and October (Fig. 9g and 9l). Here, enhanced surface fluxes will help counteract cloud thinning.

N_d changes can be expected to be most closely correlated with any changes in boundary-layer aerosol. In August and October (Fig. 9e and 9o), N_d increases over most of the stratocumulus deck and most obviously at the deck's southern and western edges, approximately collocated with positive trends in CO_{MT}. This contrasts with a clear N_d reduction in September (Fig. 9j). The increasing trend in low cloud fraction south of St. Helena Island in September and October is also collocated with increases in EIS, consistent with an increased free-tropospheric advection of warm, smoky (in September) air above the cloud. One consistent interpretation is that the aerosol may be helping to stabilize the lower free troposphere further in September, consistent with more transport occurring at higher altitudes, as captured by the CO_{MT} trend, but is not entraining into the stratocumulus deck.

Liquid water paths (LWPs) increase over all three months, but insignificantly so. A slight LWP decrease is instead documented by Jouan and Myrhe (2024) using similar datasets and time span. The explanation for the difference may be because of our focus on individual months as opposed to seasonal means, or slight differences in selected grids. The spatial pattern of more cloud at the southern edge of the stratocumulus deck is captured in both analyses as well as (Wall et al., 2023), with both Wall et al. (2023) and Jouan and Myrhe (2024) finding an overall increased outgoing top-of-atmosphere shortwave radiation (a cooling) over the southeast Atlantic over the past 20 years. All else equal, an increase in atmospheric radiative cooling will be compensated by more latent heat release through precipitation, to maintain an energy balance.

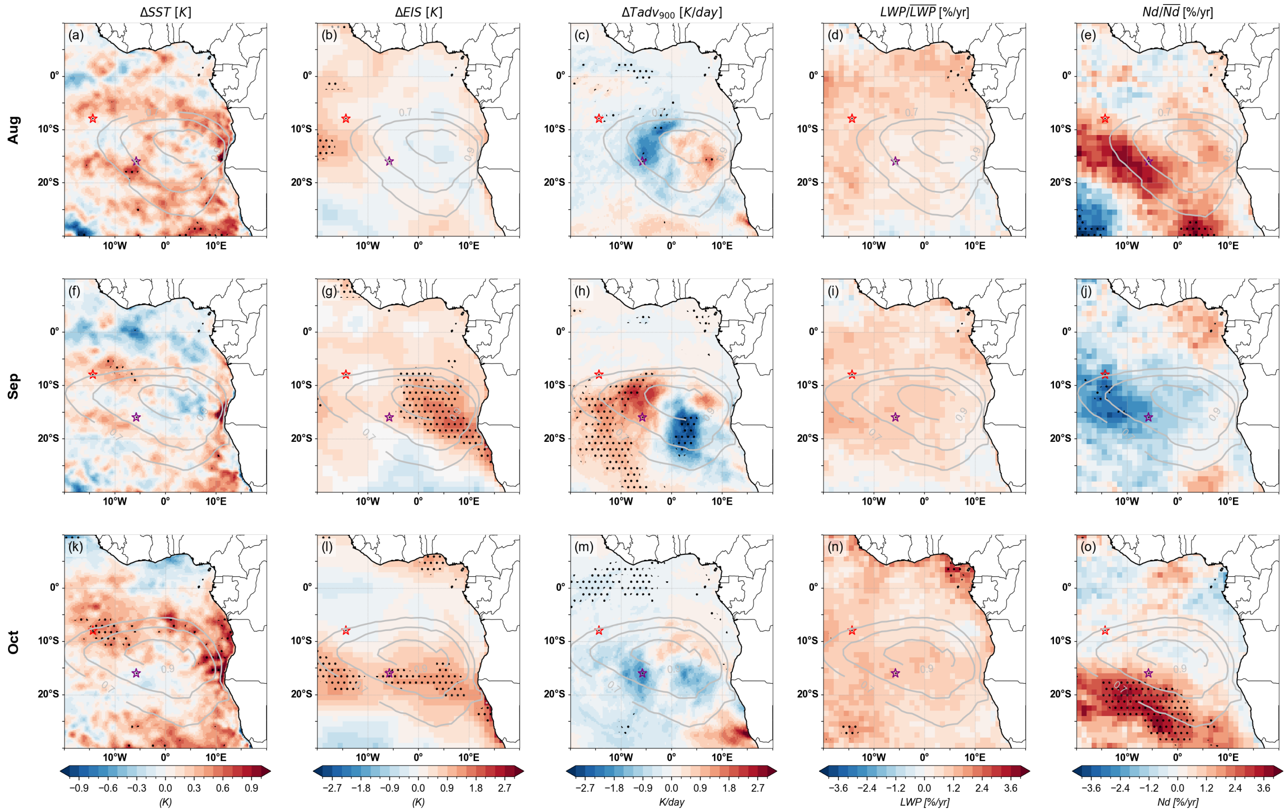

Figure 9. Recent trends (2003-2020) in ERA5 SST (first column), CERES estimated inversion strength (second column), ERA5 temperature advection at 900 hPa (third column), low cloud CERES liquid water path (fourth column), and MODIS cloud droplet number concentration (fifth column) for August (first row), September (second row), and October (third row). Stippling indicates significance at the 95% confidence levels of the trend.

4 Conclusions

By combining burned area data and meteorological reanalyses, we show early signs that the biomass burning season is starting later and is more intense in the middle of the fire season (August & September) with small fires likely contributing more over the 2003-2020 timespan. Regional differences in biomass burning suggest multiple drivers are contributing to the shift, including that burning across the continent is occurring later as an outcome of a delayed rainy season onset (Dunning et al., 2018) or an extended dry season (Zhou et al., 2014) . This doesn't explain decreased burning in Zambia in October – which we speculate is a result of earlier prescribed burnings to reduce late season wildfires (Hollingsworth et al., 2015). If detection of small fires continues to improve, and if burning changes are robustly connected to a precipitation shift, then the trend of more small fires should persist across future datasets of burned area.

More fires in August and September are combined with increases in easterly wind speeds to carry biomass burning aerosol further over the southeast Atlantic. A simple thermal wind analysis supports the deduction that land heating over Africa is a primary driver, coupled with poleward expansion to enhance the southern half of the SEA stratocumulus cloud deck. The exact mechanism behind the wind speed changes is uncertain - likely a combination of a thermal wind response and shifting seasonal meteorological controls on wind speed and low cloud cover – such as the poleward expansion of the south Atlantic subtropical high (Vizy & Cook, 2016). The combined increase in aerosol advection, with a southward shift of the stratocumulus deck, is shown to result in an increase in the net direct aerosol radiative effect (a cooling) within Jouan and Nyrhe (2024) over the southeast Atlantic, but with a spatial variation that can be explained by the changes documented here. Future works could perform mechanism denial experiments to puzzle out how future changes in the AEJ-S, biomass burning emissions taking account of their uncertainties, and clouds may affect regional climate change prediction including in precipitation.

Declaration of competing interest

The authors declare that they have no known competing financial interests or personal relationships that could have appeared to influence the work reported in this paper.

CRediT authorship contribution statement

Tyler Tatro: Conceptualization, Methodology, Software, Investigation, Formal Analysis, Writing- Original Draft, Visualization. **Paquita Zuidema**: Conceptualization, Methodology, Writing- Review & Editing, Formal Analysis, Supervision, Validation

Acknowledgements

This work is supported by the Department of Energy Atmospheric System Research award DE-SC0021250 and by NASA award 80NSSC21K1344. GFED5 burned area data are available on https://zenodo.org/records/7668424.

Fire_CCI and other burned area data from the ESA are available at https://climate.esa.int/en/projects/fire/data/. ERA5 and CAMS reanalysis are available through the ECMWF Copernicus data system. Cloud droplet number concentration data are from https://catalogue.ceda.ac.uk/uuid/864a46cc65054008857ee5bb772a2a2b. CERES data can be obtained at https://ceres.larc.nasa.gov/data/. We thank the editor and the anonymous reviewers for comments that lead to improvements in the manuscript.

References

Ackerman, A. S., Toon, O. B., Stevens, D. E., Heymsfield, A. J., Ramanathan, V., & Welton, E. J. (2000). Reduction of tropical cloudiness by soot. *Science*, *288*(5468). https://doi.org/10.1126/science.288.5468.1042

Adebiyi, A. A., & Zuidema, P. (2016). The role of the southern African easterly jet in modifying the southeast Atlantic aerosol and cloud environments. *Quarterly Journal of the Royal Meteorological Society*, *142*(697). https://doi.org/10.1002/qj.2765

Adebiyi, A. A., & Zuidema, P. (2018). Low cloud cover sensitivity to biomass-burning aerosols and meteorology over the Southeast Atlantic. *Journal of Climate*, *31*(11). https://doi.org/10.1175/JCLI-D-17-0406.1

Andela, N., Morton, D. C., Giglio, L., Chen, Y., Van Der Werf, G. R., Kasibhatla, P. S., et al. (2017). A human-driven decline in global burned area. *Science*, *356*(6345). https://doi.org/10.1126/science.aal4108

Anyamba, A., Justice, C. O., Tucker, C. J., & Mahoney, R. (2003). Seasonal to interannual variability of vegetation and fires at SAFARI 2000 sites inferred from advanced very high resolution radiometer time series data. *Journal of Geophysical Research: Atmospheres*, *108*(13). https://doi.org/10.1029/2002jd002464

Boschetti, L., Roy, D. P., Giglio, L., Huang, H., Zubkova, M., & Humber, M. L. (2019). Global validation of the collection 6 MODIS burned area product. *Remote Sensing of Environment*, *235*. https://doi.org/10.1016/j.rse.2019.111490

Bretherton, C. S., Blossey, P. N., & Uchida, J. (2007). Cloud droplet sedimentation, entrainment efficiency, and subtropical stratocumulus albedo. *Geophysical Research Letters*, *34*(3). https://doi.org/10.1029/2006GL027648

Brown, H., Liu, X., Pokhrel, R., Murphy, S., Lu, Z., Saleh, R., et al. (2021). Biomass burning aerosols in most climate models are too absorbing. *Nature Communications*, *12*(1). https://doi.org/10.1038/s41467-020-20482-9

Buchholz, R. R., Worden, H. M., Park, M., Francis, G., Deeter, M. N., Edwards, D. P., et al. (2021). Air pollution trends measured from Terra: CO and AOD over industrial, fire-prone, and background regions. *Remote Sensing of Environment*, *256*. https://doi.org/10.1016/j.rse.2020.112275

Catarino, S., Romeiras, M. M., Figueira, R., Aubard, V., Silva, J. M. N., & Pereira, J. M. C. (2020). Spatial and temporal trends of burnt area in angola: Implications for natural vegetation and protected area management. *Diversity*, *12*(8). https://doi.org/10.3390/D12080307

Ceamanos, X., Coopman, Q., George, M., Riedi, J., Parrington, M., & Clerbaux, C. (2023). Remote sensing and model analysis of biomass burning smoke transported across the Atlantic during the 2020 Western US wildfire season. *Scientific Reports*, *13*(1). https://doi.org/10.1038/s41598-023-39312-1

Che, H., Stier, P., Gordon, H., Watson-Parris, D., & Deaconu, L. (2020). The significant role of biomass burning aerosols in clouds and radiation in the South-eastern Atlantic Ocean. *Atmospheric Chemistry and Physics Discussions*, (June).

Chen, Y., Hall, J., Van Wees, D., Andela, N., Hantson, S., Giglio, L., et al. (2023). Multi-decadal trends and variability in burned area from the 5th version of the Global Fire Emissions Database (GFED5). https://doi.org/10.5194/essd-2023-182

Christensen, M. W., Jones, W. K., & Stier, P. (2020). Aerosols enhance cloud lifetime and brightness along the stratus-to-cumulus transition. *Proceedings of the National Academy of Sciences of the United States of America*, *117*(30). https://doi.org/10.1073/pnas.1921231117

Das, S., Harshvardhan, H., Bian, H., Chin, M., Curci, G., Protonotariou, A. P., et al. (2017). Biomass burning aerosol transport and vertical distribution over the South African-Atlantic region. *Journal of Geophysical Research*, *122*(12). https://doi.org/10.1002/2016JD026421

Deeter, M. N., Emmons, L. K., Francis, G. L., Edwards, D. P., Gille, J. C., Warner, J. X., et al. (2003). Operational carbon monoxide retrieval algorithm and selected results for the MOPITT instrument. *Journal of Geophysical Research: Atmospheres*, *108*(14). https://doi.org/10.1029/2002jd003186

Deeter, M. N., Edwards, D. P., Gille, J. C., & Drummond, J. R. (2007). Sensitivity of MOPITT observations to carbon monoxide in the lower troposphere. *Journal of Geophysical Research Atmospheres*, *112*(24). https://doi.org/10.1029/2007JD008929

Denjean, C., Bourrianne, T., Burnet, F., Mallet, M., Maury, N., Colomb, A., et al. (2020). Overview of aerosol optical properties over southern West Africa from DACCIWA aircraft measurements. *Atmospheric Chemistry and Physics*, *20*(8). https://doi.org/10.5194/acp-20-4735-2020

Diamond, M. S., Saide, P. E., Zuidema, P., Ackerman, A. S., Doherty, S. J., Fridlind, A. M., et al. (2022). Cloud adjustments from large-scale smoke-circulation interactions strongly modulate the southeastern Atlantic stratocumulus-to-cumulus transition. *Atmospheric Chemistry and Physics*, *22*(18). https://doi.org/10.5194/acp-22-12113-2022

Ding, S., & Liu, D. (2022). Evaluation of the CAMS reanalysis for atmospheric black carbon and carbon monoxide over the north China plain. *Environmental Pollution*, *314*. https://doi.org/10.1016/j.envpol.2022.120286

Dunning, C. M., Black, E., & Allan, R. P. (2018). Later wet seasons with more intense rainfall over Africa under future climate change. *Journal of Climate*, *31*(23). https://doi.org/10.1175/JCLI-D-18-0102.1

Edwards, D. P., Emmons, L. K., Gille, J. C., Chu, A., Attié, J. L., Giglio, L., et al. (2006). Satellite-observed pollution from Southern Hemisphere biomass burning. *Journal of Geophysical Research Atmospheres*, *111*(14). https://doi.org/10.1029/2005JD006655

Field, R. D., Van Der Werf, G. R., Fanin, T., Fetzer, E. J., Fuller, R., Jethva, H., et al. (2016). Indonesian fire activity and smoke pollution in 2015 show persistent nonlinear sensitivity to El Niño-induced drought. *Proceedings of the National Academy of Sciences of the United States of America*, *113*(33). https://doi.org/10.1073/pnas.1524888113

Formenti, P., D'Anna, B., Flamant, C., Mallet, M., Piketh, S. J., Schepanski, K., et al. (2019). The aerosols, radiation and clouds in southern Africa field campaign in Namibia overview, illustrative observations, and way forward. *Bulletin of the American Meteorological Society*, *100*(7). https://doi.org/10.1175/BAMS-D-17-0278.1

Gareth, R., Roberts, G., Wooster, M. J., & Lagoudakis, E. (2009). Annual and diurnal african biomass burning temporal dynamics. *Biogeosciences*, *6*(5). https://doi.org/10.5194/bg-6-849-2009

Gelaro, R., McCarty, W., Suárez, M. J., Todling, R., Molod, A., Takacs, L., et al. (2017). The modern-era retrospective analysis for research and applications, version 2 (MERRA-2). *Journal of Climate*, *30*(14). https://doi.org/10.1175/JCLI-D-16-0758.1

Giglio, L., Descloitres, J., Justice, C. O., & Kaufman, Y. J. (2003). An enhanced contextual fire detection algorithm for MODIS. *Remote Sensing of Environment*, *87*(2–3). https://doi.org/10.1016/S0034-4257(03)00184-6

Giglio, L., Csiszar, I., & Justice, C. O. (2006). Global distribution and seasonality of active fires as observed with the Terra and Aqua Moderate Resolution Imaging Spectroradiometer (MODIS) sensors. *Journal of Geophysical Research: Biogeosciences*, *111*(2). https://doi.org/10.1029/2005JG000142

Giglio, L., Boschetti, L., Roy, D. P., Humber, M. L., & Justice, C. O. (2018). The Collection 6 MODIS burned area mapping algorithm and product. *Remote Sensing of Environment*, *217*. https://doi.org/10.1016/j.rse.2018.08.005

Gordon, H., Field, P. R., Abe, S. J., Dalvi, M., Grosvenor, D. P., Hill, A. A., et al. (2018). Large simulated radiative effects of smoke in the south-east Atlantic. *Atmospheric Chemistry and Physics*, *18*(20). https://doi.org/10.5194/acp-18-15261-2018

Griffin, D., Chen, J., Anderson, K., Makar, P., Mclinden, C. A., Dammers, E., et al. (n.d.). Towards an improved understanding of wildfire CO emissions: a satellite remote-sensing perspective. https://doi.org/10.5194/egusphere-2023-649

Gryspeerdt, E., McCoy, D. T., Crosbie, E., Moore, R. H., Nott, G. J., Painemal, D., et al. (2022). The impact of sampling strategy on the cloud droplet number concentration estimated from satellite data. *Atmospheric Measurement Techniques*, *15*(12). https://doi.org/10.5194/amt-15-3875-2022

Hansen, J., Sato, M., & Ruedy, R. (1997). Radiative forcing and climate response. *Journal of Geophysical Research Atmospheres*, *102*(D6). https://doi.org/10.1029/96JD03436

Haywood, J. M., Abel, S. J., Barrett, P. A., Bellouin, N., Blyth, A., Bower, K. N., et al. (2021). The CLoud-Aerosol-Radiation Interaction and Forcing: Year 2017 (CLARIFY-2017) measurement campaign. *Atmospheric Chemistry and Physics*, *21*(2). https://doi.org/10.5194/acp-21-1049-2021

Herbert, R. J., Bellouin, N., Highwood, E. J., & Hill, A. A. (2020). Diurnal cycle of the semi-direct effect from a persistent absorbing aerosol layer over marine stratocumulus in large-eddy simulations. *Atmospheric Chemistry and Physics*, *20*(3). https://doi.org/10.5194/acp-20-1317-2020

Hersbach, H., Bell, B., Berrisford, P., Hirahara, S., Horányi, A., Muñoz-Sabater, J., et al. (2020). The ERA5 global reanalysis. *Quarterly Journal of the Royal Meteorological Society*, *146*(730). https://doi.org/10.1002/qj.3803

Holloway, T., Levy, H., & Kasibhatla, P. (2000). Global distribution of carbon monoxide. *Journal of Geophysical Research Atmospheres*, *105*(D10). https://doi.org/10.1029/1999JD901173

Inness, A., Ades, M., Agustí-Panareda, A., Barr, J., Benedictow, A., Blechschmidt, A. M., et al. (2019). The CAMS reanalysis of atmospheric composition. *Atmospheric Chemistry and Physics*, *19*(6). https://doi.org/10.5194/acp-19-3515-2019

Inness, A., Aben, I., Ades, M., Borsdorff, T., Flemming, J., Jones, L., et al. (2022). Assimilation of S5P/TROPOMI carbon monoxide data with the global CAMS near-real-time system. *Atmospheric Chemistry and Physics*, *22*(21). https://doi.org/10.5194/acp-22-14355-2022

Jiang, Y., Zhou, L., & Raghavendra, A. (2020). Observed changes in fire patterns and possible drivers over Central Africa. *Environmental Research Letters*, *15*(9). https://doi.org/10.1088/1748-9326/ab9db2

Johansson, S., Wetzel, G., Friedl-Vallon, F., Glatthor, N., Höpfner, M., Kleinert, A., et al. (2022). Biomass burning pollution in the South Atlantic upper troposphere: GLORIA trace gas observations and evaluation of the CAMS model. *Atmospheric Chemistry and Physics*, *22*(5). https://doi.org/10.5194/acp-22-3675-2022

Johnson, B. T., Shine, K. P., & Forster, P. M. (2004). The semi-direct aerosol effect: Impact of absorbing aerosols on marine stratocumulus. *Quarterly Journal of the Royal Meteorological Society*, *130*(599 PART B). https://doi.org/10.1256/qj.03.61

Jouan, C., & Myhre, G. (2024). Satellite-based analysis of top of atmosphere shortwave radiative forcing trend induced by biomass burning aerosols over South-Eastern Atlantic. *Npj Climate and Atmospheric Science*, *7*(1). https://doi.org/10.1038/s41612-024-00631-3

Kacarab, M., Lee Thornhill, K., Dobracki, A., Howell, S. G., O'Brien, J. R., Freitag, S., et al. (2020). Biomass burning aerosol as a modulator of the droplet number in the southeast Atlantic region. *Atmospheric Chemistry and Physics*, *20*(5). https://doi.org/10.5194/acp-20-3029-2020

Kaiser, J. W., Heil, A., Andreae, M. O., Benedetti, A., Chubarova, N., Jones, L., et al. (2012). Biomass burning emissions estimated with a global fire assimilation system based on observed fire radiative power. *Biogeosciences*. https://doi.org/10.5194/bg-9-527-2012

Korontzi, S. (2005). Seasonal patterns in biomass burning emissions from southern African vegetation fires for the year 2000. *Global Change Biology*, *11*(10). https://doi.org/10.1111/j.1365-2486.2005.001024.x

Kuete, G., Pokam Mba, W., & Washington, R. (2020). African Easterly Jet South: control, maintenance mechanisms and link with Southern subtropical waves. *Climate Dynamics*, *54*(3–4). https://doi.org/10.1007/s00382-019-05072-w

Kuete, G., Mba, W. P., James, R., Dyer, E., Annor, T., & Washington, R. (2023). How do coupled models represent the African Easterly Jets and their associated dynamics over Central Africa during the September–November rainy season? *Climate Dynamics*, *60*(9–10). https://doi.org/10.1007/s00382-022-06467-y

Liousse, C., Assamoi, E., Criqui, P., Granier, C., & Rosset, R. (2014). Explosive growth in African combustion emissions from 2005 to 2030. *Environmental Research Letters*, *9*(3). https://doi.org/10.1088/1748-9326/9/3/035003

Lizundia-Loiola, J., Otón, G., Ramo, R., & Chuvieco, E. (2020). A spatio-temporal active-fire clustering approach for global burned area mapping at 250 m from MODIS data. *Remote Sensing of Environment*, *236*. https://doi.org/10.1016/j.rse.2019.111493

Lu, J., Vecchi, G. A., & Reichler, T. (2007). Expansion of the Hadley cell under global warming. *Geophysical Research Letters*, *34*(6). https://doi.org/10.1029/2006GL028443

Lu, Z., Liu, X., Zhang, Z., Zhao, C., Meyer, K., Rajapakshe, C., et al. (2018). Biomass smoke from southern Africa can significantly enhance the brightness of stratocumulus over the southeastern Atlantic Ocean. *Proceedings of the National Academy of Sciences of the United States of America*, *115*(12). https://doi.org/10.1073/pnas.1713703115

Mallet, M., Nabat, P., Johnson, B., Michou, M., Haywood, J. M., Chen, C., & Dubovik, O. (2021). Climate models generally underrepresent the warming by central africa biomass-burning aerosols over the southeast atlantic. *Science Advances*, *7*(41). https://doi.org/10.1126/sciadv.abg9998

Manney, G. L., & Hegglin, M. I. (2018). Seasonal and regional variations of long-term changes in upper-tropospheric jets from reanalyses. *Journal of Climate*, *31*(1). https://doi.org/10.1175/JCLI-D-17-0303.1

Moriconi-Ebrard, F., Harre, D., & Heinrigs, P. (2016). *Urbanisation Dynamics in West Africa 1950–2010. OECD*.

Nicholson, S. E., & Grist, J. P. (2003). The seasonal evolution of the atmospheric circulation over West Africa and equatorial Africa. *Journal of Climate*, *16*(7). https://doi.org/10.1175/1520-0442(2003)016<1013:TSEOTA>2.0.CO;2

Novelli, P. C., Masarie, K. A., Lang, P. M., Hall, B. D., Myers, R. C., & Elkins, J. W. (2003). Reanalysis of tropospheric CO trends: Effects of the 1997-1998 wildfires. *Journal of Geophysical Research: Atmospheres*, *108*(15). https://doi.org/10.1029/2002jd003031

Pan, X., Ichoku, C., Chin, M., Bian, H., Darmenov, A., Colarco, P., et al. (2020). Six global biomass burning emission datasets: Intercomparison and application in one global aerosol model. *Atmospheric Chemistry and Physics*, *20*(2). https://doi.org/10.5194/acp-20-969-2020

Phiri, D., Mwitwa, J., Ng'andwe, P., Kanja, K., Munyaka, J., Chileshe, F., et al. (2023). Agricultural expansion into forest reserves in Zambia: a remote sensing approach. *Geocarto International*, *38*(1). https://doi.org/10.1080/10106049.2023.2213203

Pistone, K., Wilcox, E. M., Zuidema, P., Giordano, M., Podolske, J., Leblanc, S. E., et al. (n.d.). Vertical structure of a springtime smoky and humid troposphere over the Southeast Atlantic from aircraft and reanalysis. https://doi.org/10.5194/egusphere-2023-2412

Ract, C., Burgess, N. D., Dinesen, L., Sumbi, P., Malugu, I., Latham, J., et al. (2024). Nature Forest Reserves in Tanzania and their importance for conservation. *PLoS ONE*, *19*(2 February). https://doi.org/10.1371/journal.pone.0281408

Ramo, R., Roteta, E., Bistinas, I., van Wees, D., Bastarrika, A., Chuvieco, E., & van der Werf, G. R. (2021). African burned area and fire carbon emissions are strongly impacted by small fires undetected by coarse resolution satellite data. *Proceedings of the National Academy of Sciences of the United States of America*, *118*(9). https://doi.org/10.1073/pnas.2011160118

Redemann, J., Wood, R., Zuidema, P., Doherty, S. J., Luna, B., LeBlanc, S. E., et al. (2021, February 4). An overview of the ORACLES (ObseRvations of aerosols above CLouds and their intEractionS) project: Aerosol-cloud-radiation interactions in the southeast Atlantic basin. *Atmospheric Chemistry and Physics*. Copernicus GmbH. https://doi.org/10.5194/acp-21-1507-2021

Roteta, E., Bastarrika, A., Padilla, M., Storm, T., & Chuvieco, E. (2019). Development of a Sentinel-2 burned area algorithm: Generation of a small fire database for sub-Saharan Africa. *Remote Sensing of Environment*, *222*. https://doi.org/10.1016/j.rse.2018.12.011

Ryoo, J. M., Pfister, L., Ueyama, R., Zuidema, P., Wood, R., Chang, I., & Redemann, J. (2021). A meteorological overview of the ORACLES (ObseRvations of Aerosols above CLouds and their intEractionS) campaign over the southeastern Atlantic during 2016-2018: Part 1 - Climatology. *Atmospheric Chemistry and Physics*, *21*(22). https://doi.org/10.5194/acp-21-16689-2021

Scott, R. C., Myers, T. A., Norris, J. R., Zelinka, M. D., Klein, S. A., Sun, M., & Doelling, D. R. (2020). Observed sensitivity of low-cloud radiative effects to meteorological perturbations over the global oceans. *Journal of Climate*, *33*(18). https://doi.org/10.1175/JCLI-D-19-1028.1

Seethala, C., Norris, J. R., & Myers, T. A. (2015). How has subtropical stratocumulus and associated meteorology changed since the 1980s? *Journal of Climate*, *28*(21). https://doi.org/10.1175/JCLI-D-15-0120.1

Twomey, S. (1977). The Influence of Pollution on the Shortwave Albedo of Clouds. *Journal of the Atmospheric Sciences*, *34*(7). https://doi.org/10.1175/1520-0469(1977)034<1149:tiopot>2.0.co;2

Tyukavina, A., Hansen, M. C., Potapov, P., Parker, D., Okpa, C., Stehman, S. V., et al. (2018). Congo Basin forest loss dominated by increasing smallholder clearing. *Science Advances*, *4*(11). https://doi.org/10.1126/sciadv.aat2993

United Nations High Commissioner for Refugees. (2023). *Angola Registration Report 2023*. Retrieved from https://data.unhcr.org/en/documents/details/100903

van der Velde, I. R., van der Werf, G. R., van Wees, D., Schutgens, N. A. J., Vernooij, R., Houweling, S., et al. (2024). Small Fires, Big Impact: Evaluating Fire Emission Estimates in Southern Africa Using New Satellite Imagery of Burned Area and Carbon Monoxide. *Geophysical Research Letters*, *51*(12). https://doi.org/10.1029/2023GL106122

Vizy, E. K., & Cook, K. H. (2016). Understanding long-term (1982–2013) multi-decadal change in the equatorial and subtropical South Atlantic climate. *Climate Dynamics*, *46*(7–8). https://doi.org/10.1007/s00382-015-2691-1

Wall, C. J., Storelvmo, T., & Possner, A. (2023). Global observations of aerosol indirect effects from marine liquid clouds. *Atmospheric Chemistry and Physics*, *23*(20). https://doi.org/10.5194/acp-23-13125-2023

Wang, Z., Chappellaz, J., Park, K., & Mak, J. E. (2010). Large variations in southern hemisphere biomass burning during the last 650 years. *Science*, *330*(6011). https://doi.org/10.1126/science.1197257

Ward, D. E., Hao, W. M., Susott, R. A., Babbitt, R. E., Shea, R. W., Kauffman, J. B., & Justice, C. O. (1996). Effect of fuel composition on combustion efficiency and emission factors for African savanna ecosystems. *Journal of Geophysical Research Atmospheres*, *101*(19). https://doi.org/10.1029/95jd02595

van Wees, D., van der Werf, G. R., Randerson, J. T., Andela, N., Chen, Y., & Morton, D. C. (2021). The role of fire in global forest loss dynamics. *Global Change Biology*, *27*(11). https://doi.org/10.1111/gcb.15591

Van Wees, D., Van Der Werf, G. R., Randerson, J. T., Rogers, B. M., Chen, Y., Veraverbeke, S., et al. (2022). Global biomass burning fuel consumption and emissions at 500 m spatial resolution based on the Global Fire Emissions Database (GFED). *Geoscientific Model Development*, *15*(22). https://doi.org/10.5194/gmd-15-8411-2022

Van Der Werf, G. R., Randerson, J. T., Giglio, L., Collatz, G. J., Kasibhatla, P. S., & Arellano, A. F. (2006). Interannual variability in global biomass burning emissions from 1997 to 2004. *Atmospheric Chemistry and Physics*, *6*(11). https://doi.org/10.5194/acp-6-3423-2006

Van Der Werf, G. R., Randerson, J. T., Giglio, L., Collatz, G. J., Mu, M., Kasibhatla, P. S., et al. (2010). Global fire emissions and the contribution of deforestation, savanna, forest, agricultural, and peat fires (1997-2009). *Atmospheric Chemistry and Physics*, *10*(23). https://doi.org/10.5194/acp-10-11707-2010

Wiedinmyer, C., Kimura, Y., Mcdonald-Buller, E. C., Emmons, L. K., Buchholz, R. R., Tang, W., et al. (2023). The Fire Inventory from NCAR version 2.5: an updated global fire emissions model for climate and chemistry applications. *Geoscientific Model Development*, *16*(13). https://doi.org/10.5194/gmd-16-3873-2023

Wielicki, B. A., Barkstrom, B. R., Harrison, E. F., Lee, R. B., Smith, G. L., & Cooper, J. E. (1996). Clouds and the Earth’s Radiant Energy System (CERES): An Earth Observing System Experiment. *Bulletin of the American Meteorological Society*, *77*(5). https://doi.org/10.1175/1520-0477(1996)077<0853:CATERE>2.0.CO;2

van Wilgen, B. W., Everson, C. S., & Trollope, W. S. W. (1990). Fire Management in Southern Africa: Some Examples of Current Objectives, Practices, and Problems. https://doi.org/10.1007/978-3-642-75395-4_11

Wimberly, M. C., Wanyama, D., Doughty, R., Peiro, H., & Crowell, S. (2024). Increasing Fire Activity in African Tropical Forests Is Associated With Deforestation and Climate Change. *Geophysical Research Letters*, *51*(9). https://doi.org/10.1029/2023GL106240

Winker, D. M., Vaughan, M. A., Omar, A., Hu, Y., Powell, K. A., Liu, Z., et al. (2009). Overview of the CALIPSO mission and CALIOP data processing algorithms. *Journal of Atmospheric and Oceanic Technology*, *26*(11). https://doi.org/10.1175/2009JTECHA1281.1

Wolski, P., Conradie, S., Jack, C., & Tadross, M. (2021). Spatio-temporal patterns of rainfall trends and the 2015–2017 drought over the winter rainfall region of South Africa. *International Journal of Climatology*, *41*(S1). https://doi.org/10.1002/joc.6768

Wood, R., & Bretherton, C. S. (2006). On the relationship between stratiform low cloud cover and lower-tropospheric stability. *Journal of Climate*, *19*(24). https://doi.org/10.1175/JCLI3988.1

Woollings, T., Drouard, M., O’Reilly, C. H., Sexton, D. M. H., & McSweeney, C. (2023). Trends in the atmospheric jet streams are emerging in observations and could be linked to tropical warming. *Communications Earth and Environment*, *4*(1). https://doi.org/10.1038/s43247-023-00792-8

Wu, H., Taylor, J. W., Szpek, K., Langridge, J. M., Williams, P. I., Flynn, M., et al. (2020). Vertical variability of the properties of highly aged biomass burning aerosol transported over the southeast Atlantic during CLARIFY-2017. *Atmospheric Chemistry and Physics*, *20*(21). https://doi.org/10.5194/acp-20-12697-2020

Yurganov, L., McMillan, W., Grechko, E., & Dzhola, A. (2010). Analysis of global and regional co burdens measured from space between 2000 and 2009 and validated by ground-based solar tracking spectrometers. *Atmospheric Chemistry and Physics*, *10*(8). https://doi.org/10.5194/acp-10-3479-2010

Zhang, J., & Feingold, G. (2023). Distinct regional meteorological influences on low-cloud albedo susceptibility over global marine stratocumulus regions. *Atmospheric Chemistry and Physics*, *23*(2). https://doi.org/10.5194/acp-23-1073-2023

Zhang, J., & Zuidema, P. (2019). The diurnal cycle of the smoky marine boundary layer observed during August in the remote southeast Atlantic. *Atmospheric Chemistry and Physics*, *19*(23). https://doi.org/10.5194/acp-19-14493-2019

Zhang, J., & Zuidema, P. (2021). Sunlight-absorbing aerosol amplifies the seasonal cycle in low-cloud fraction over the southeast Atlantic. *Atmospheric Chemistry and Physics*, *21*(14). https://doi.org/10.5194/acp-21-11179-2021

Zheng, B., Chevallier, F., Ciais, P., Yin, Y., & Wang, Y. (2018). On the Role of the Flaming to Smoldering Transition in the Seasonal Cycle of African Fire Emissions. *Geophysical Research Letters*, *45*(21). https://doi.org/10.1029/2018GL079092

Zheng, B., Chevallier, F., Yin, Y., Ciais, P., Fortems-Cheiney, A., Deeter, M. N., et al. (2019). Global atmospheric carbon monoxide budget 2000-2017 inferred from multi-species atmospheric inversions. *Earth System Science Data*, *11*(3). https://doi.org/10.5194/essd-11-1411-2019

Zhou, L., Tian, Y., Myneni, R. B., Ciais, P., Saatchi, S., Liu, Y. Y., et al. (2014). Widespread decline of Congo rainforest greenness in the past decade. *Nature*, *508*(7498). https://doi.org/10.1038/nature13265

Zuidema, P., Sedlacek, A. J., Flynn, C., Springston, S., Delgadillo, R., Zhang, J., et al. (2018). The Ascension Island Boundary Layer in the Remote Southeast Atlantic is Often Smoky. *Geophysical Research Letters*, *45*(9). https://doi.org/10.1002/2017GL076926

x

Supplement of

More biomass burning aerosol is being advected westward over the southern tropical Atlantic since 2003

By Tyler Tatro and Paquita Zuidema

*Correspondence to Tyler Tatro (tyler.tatro@miami.edu)
Rosenstiel School of Marine, Atmospheric, and Earth Science, University of Miami, Miami, FL, USA.

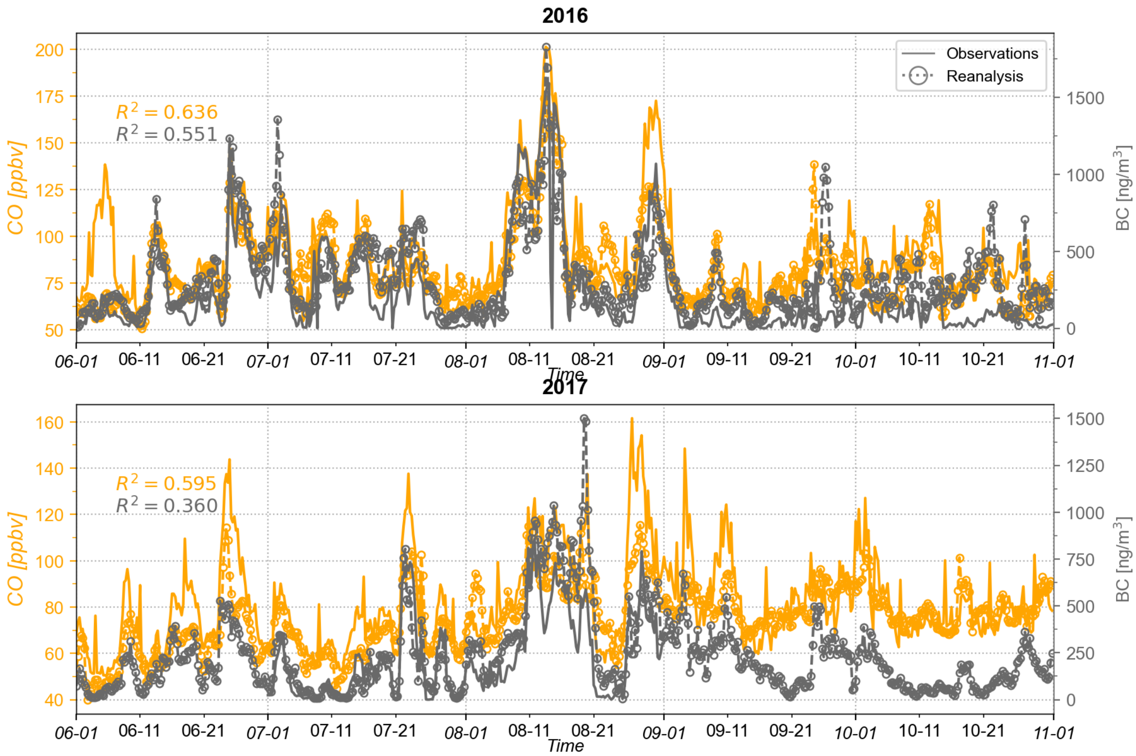

Figure **S1.** Comparison of CAMS CO and black carbon values to LASIC observations at Ascension Island (8°S, 14.5°W) for June through October in 2016 (top panel) and 2017 (bottom panel).

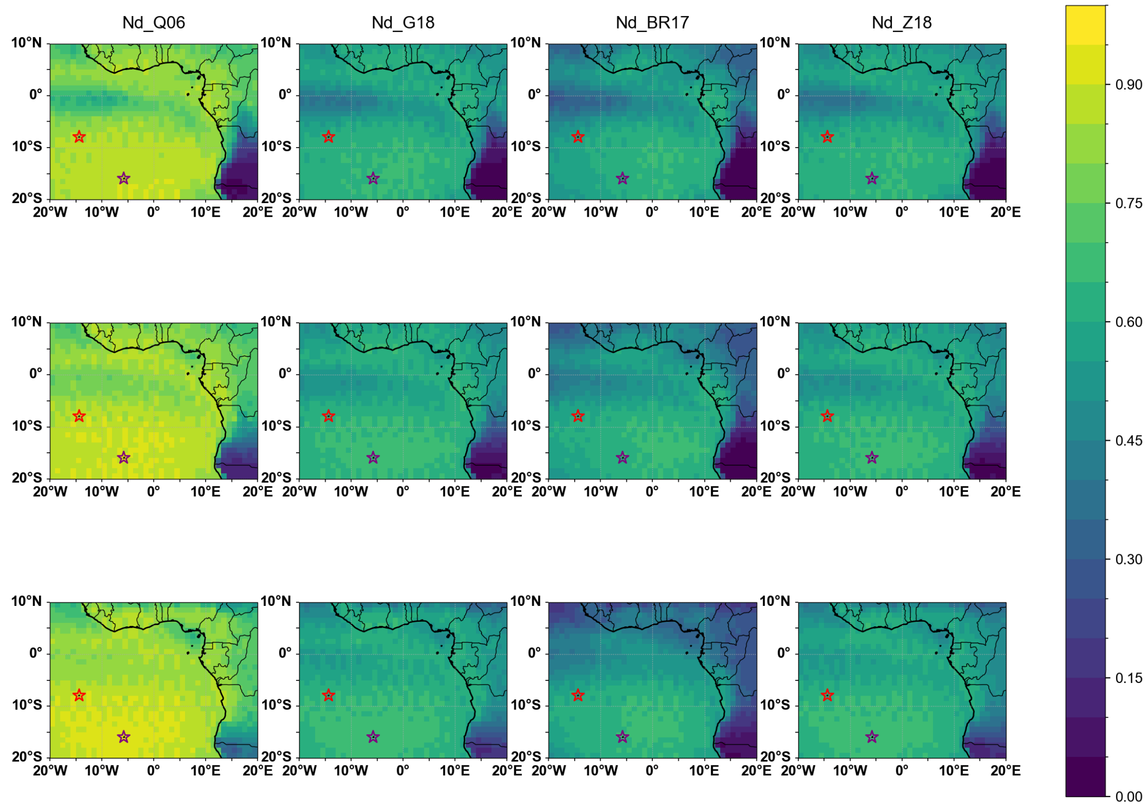

Figure S2. Temporal coverage of N_d datasets in August (top row), September (middle row) and October (bottom row).

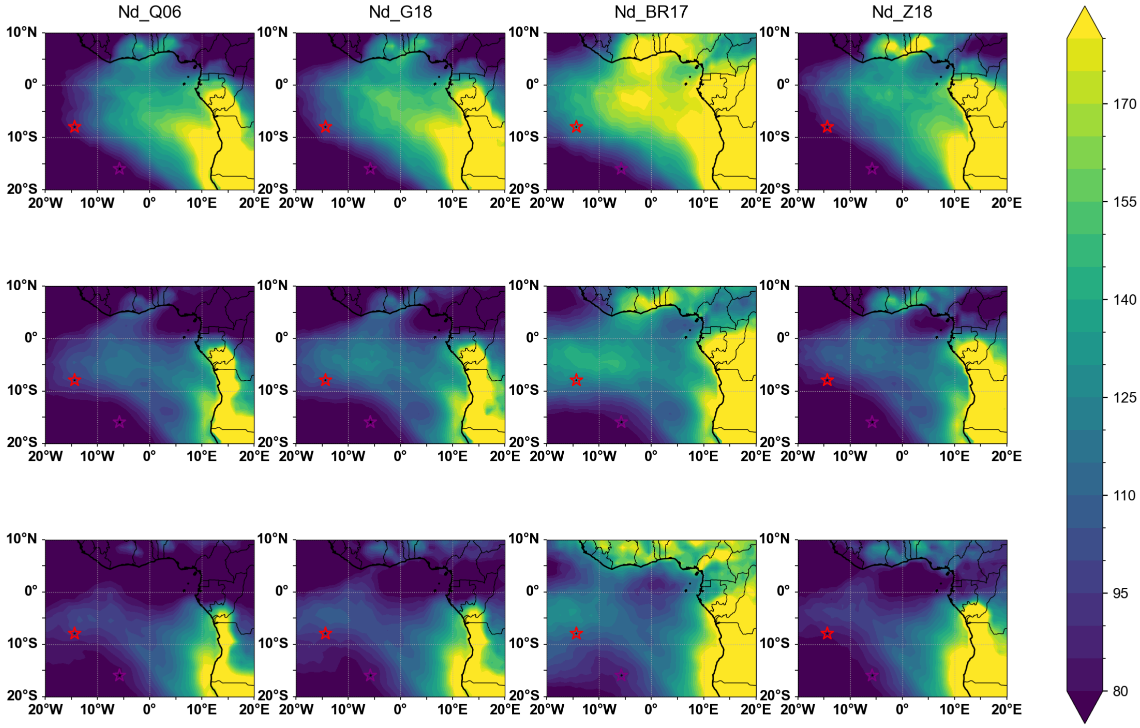

Figure S3. Average of N_d datasets in August (top row), September (middle row) and October (bottom row).

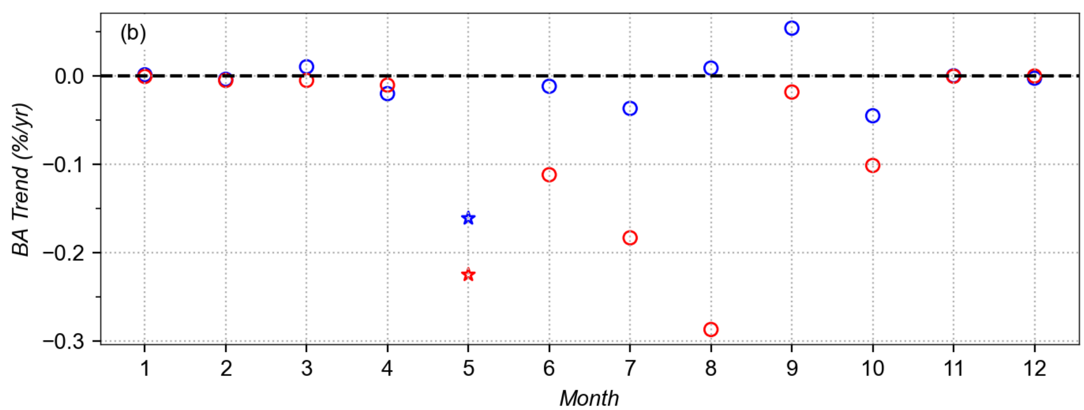

Figure S4. Difference in total burned area trends between GFED5 (blue circles) and Fire_CCI (red circles) normalized by the respective monthly average. Trends are averaged over 12-40°W and 0-30°S, for the period 2003-2020. The only trends significant at the 95% confidence level (marked as stars) are in May in both datasets.

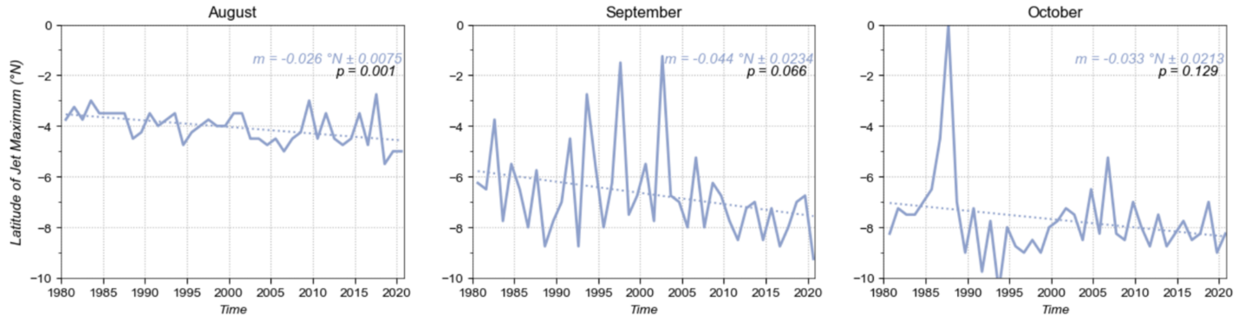

Figure S5. Time series of ERA5 latitude of AEJ-S maximum easterly wind speed (minimum u-wind).

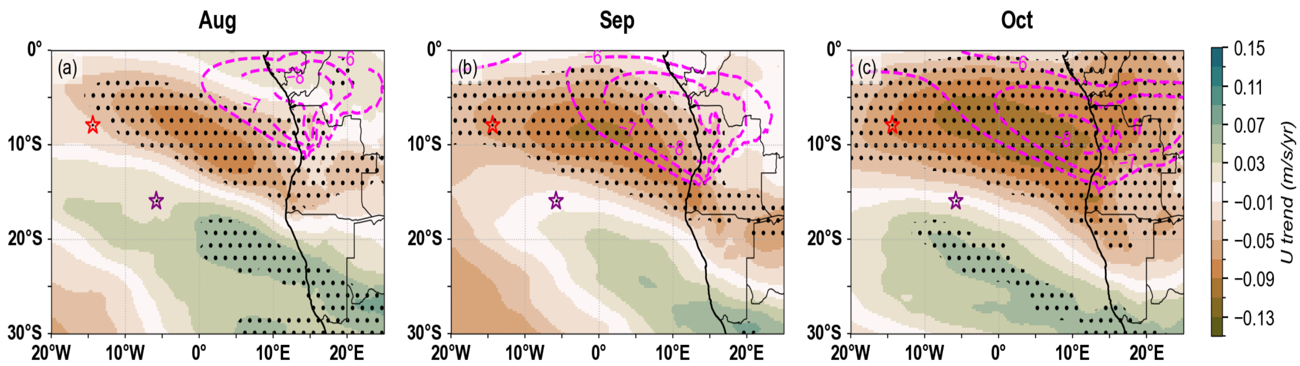

Figure S6. Trend in ERA5 zonal wind (shading) at 700 hPa, 600 hPa, and 600 hPa. Stippling indicates significance at the 95% confidence levels. Pink contours (-6, -7, -8 m/s) show the mean AEJ-S location.

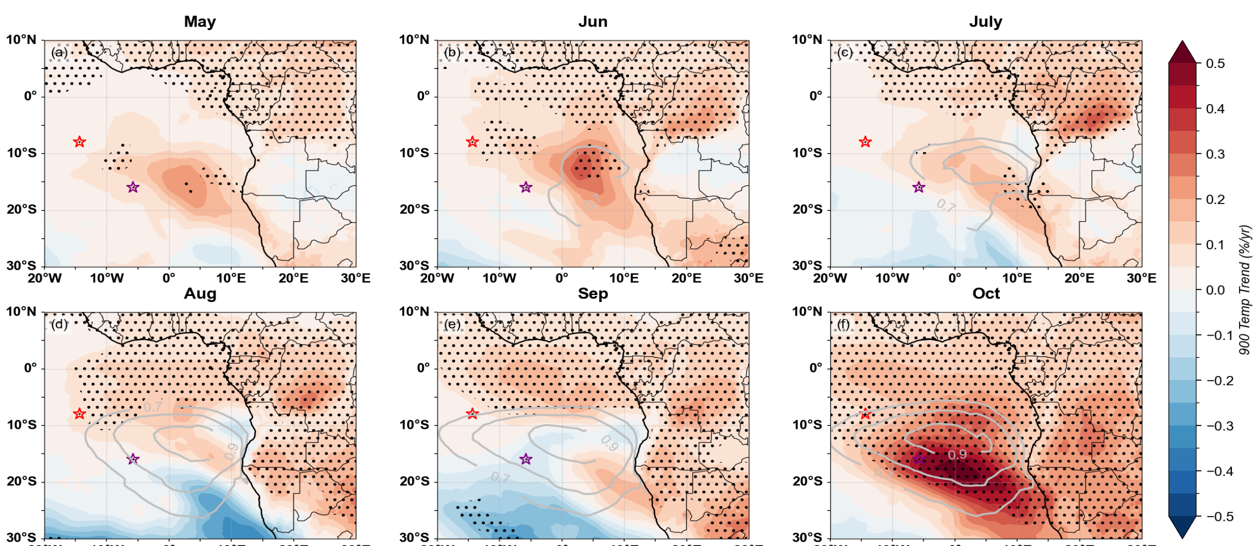

Figure S7. Trend in 900 hPa ERA5 temperature (shading) normalized by the monthly mean temperature, displayed with monthly mean cloud fraction (gray lines, 0.7-0.9). Stippling indicates significance at the 95% confidence levels.

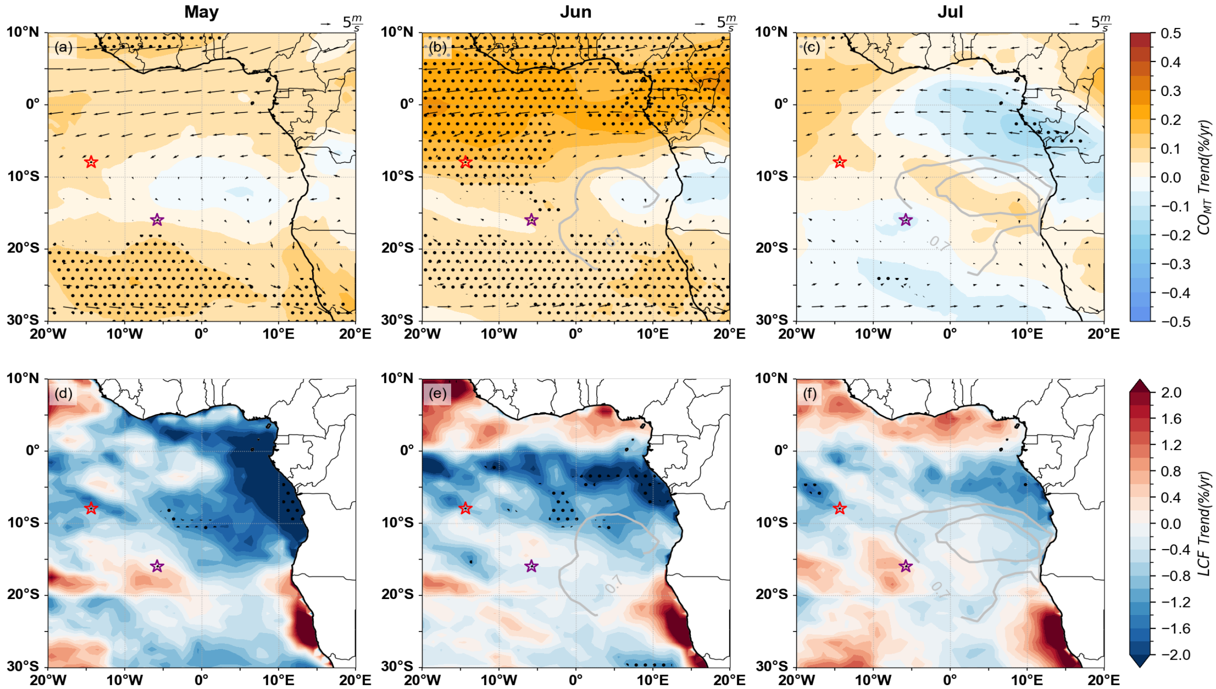

Figure S8. Residual trend in CO_{MT} for a) May b) June, and c) July (shaded) expressed as a percentage of the CO column mean, shown with the mean circulation at 700 hPa (vectors) and mean low cloud fraction (gray contours, 0.7-0.9) for 2003-2022 (a-c). Panels d-f indicate the corresponding trend in CERES low cloud fraction. Stippling indicates significance of the regression line at the 95% confidence level. Ascension and St. Helena islands indicated (light and dark red stars).

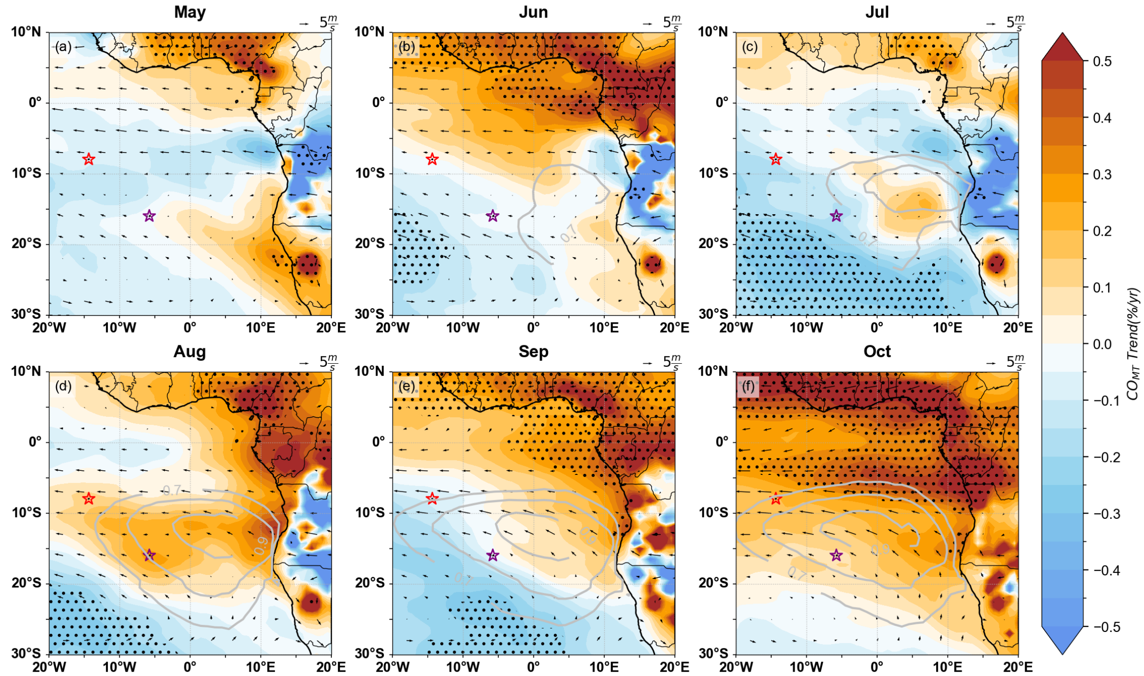

Figure S9. Residual trends in CO_{LT} for May to Otcober (shaded) expressed as a percentage of the CO column mean, shown with mean circulation at 800 hPa (vectors) and mean low cloud fraction (gray contours, 0.7-0.9) for 2003-2022 (a-e). Stippling indicates significance of the regression line at the 95% confidence level. Ascension and St. Helena islands indicated (light and dark red stars).

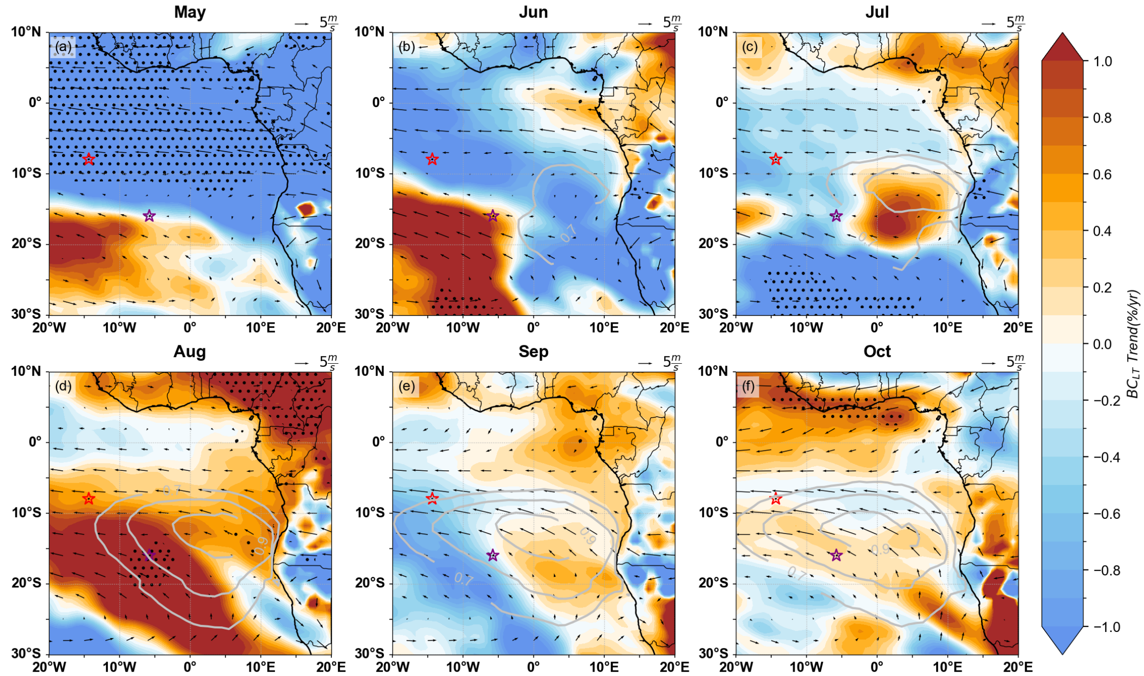

Figure S10. Trends in BC_{LT} for May to October (shaded) expressed as a percentage of the BC column mean, shown with mean circulation at 800 hPa (vectors) and mean low cloud fraction (gray contours, 0.7-0.9) for 2003-2022 (a-e). Stippling indicates significance of the regression line at the 95% confidence level. Ascension and St. Helena islands indicated (light and dark red stars).